Mutations in unfolded protein response regulator ATF6 cause hearing and vision loss syndrome

Eun-Jin Lee[1,2,3], Kyle Kim[1,3], Monica Sophia Diaz-Aguilar[1,2,3,4], Hyejung Min[2,3], Eduardo Chavez[5], Korina J. Steinbergs[1,2], Lance A. Safarta[1,2], Guirong Zhang[1,3], Allen F. Ryan[5], and Jonathan H. Lin[1,2,3*]

[1] Pathology, Stanford University School of Medicine, Stanford, CA, United States

[2] Ophthalmology, Stanford University School of Medicine, Stanford, CA, United States

[3] VA Palo Alto Healthcare System, Palo Alto, CA, United States.

[4] Rush University Medical College, Chicago, IL, United States.

[5] Departments of Otolaryngology and Neuroscience, University of California San Diego and Veterans Administration Medical Center, La Jolla, CA, United States

Address correspondence to:

[†]Jonathan Lin, School of Medicine, Stanford University, 300 Pasteur Dr. L235, Palo Alto, CA 94305, USA; Phone (650) 497-3018; email: Jonathan.H.Lin@stanford.edu

Conflict of interest:

The authors declare no competing interests.

Abstract

Activating transcription factor 6 (Atf6) is a key regulator of the unfolded protein response (UPR) and is important for endoplasmic reticulum (ER) function and protein homeostasis in metazoan cells. Patients carrying loss-of-function *ATF6* disease alleles develop the cone dysfunction disorder, achromatopsia. The impact of loss of ATF6 function on other cell types, organs, and diseases in people remains unclear. Here, we reported that progressive sensorineural hearing loss was a notable complaint in some patients carrying *ATF6* disease alleles and that *Atf6*$^{-/-}$ mice also showed progressive auditory deficits affecting both genders. In mice with hearing deficits, we found disorganized stereocilia on hair cells and focal loss of outer hair cells. Transcriptomic analysis of *Atf6*$^{-/-}$ cochleae revealed marked induction of UPR, especially through the PERK arm. These findings identify ATF6 as an essential regulator of cochlear health and function. Furthermore, they supported that ATF6 inactivation in people causes progressive sensorineural hearing loss as part of a blindness-deafness genetic syndrome targeting hair cells and cone photoreceptors. Lastly, our genetic findings support ER stress as an important pathomechanism underlying cochlear damage and hearing loss with clinical implications for patient lifestyle modifications that minimize environmental/physiologic sources of ER stress to the ear.

Introduction

Activating Transcription Factor 6 (ATF6) encodes a glycosylated 670-amino acid type II endoplasmic reticulum (ER) transmembrane protein that regulates a signal transduction pathway of the Unfolded Protein Response (UPR) (1, 2). In response to ER stress, ATF6 protein migrates from the ER to the Golgi apparatus where Golgi-resident Site 1 and Site 2 proteases cleave the ATF6 transmembrane domain and liberate the cytosolic bZIP transcription factor domain (3, 4). The liberated ATF6 bZIP-transcription factor domain enters the nucleus and upregulates ER chaperones, ER protein folding enzymes, and ER-associated degradation (ERAD) components (1, 5-8). Thus, ATF6 signaling helps cells adapt to ER stress by enhancing ER protein folding functions and maintaining ER protein quality (2, 9).

In people, we previously identified many ATF6 alleles that disrupt ATF6 signaling (10-13). These include missense variants in the luminal domain of ATF6 that impair ER-to-Golgi trafficking of the full-length ATF6 protein (11, 12); missense variants in the bZIP DNA-binding domain of ATF6 (10, 11); premature stop codons and splice-site variants (10, 13); as well as large multi-exon deletions at the ATF6 locus (13). Fibroblasts and stem cells from people carrying these ATF6 alleles, and expression of recombinant ATF6 variant proteins in HEK293 cells, all revealed loss of ATF6 transcriptional activity (10, 13-15). Individuals who are homozygous or compound heterozygous for these variants have congenital vision loss diseases, achromatopsia and cone-rod dystrophy (10, 12, 13, 16, 17). Patient retinas and retinal organoids differentiated from patient iPSCs or from *Atf6*$^{-/-}$ hESCs generated by CRISPR deletion revealed absence of outer segments, the organelle responsible for phototransduction, on cone photoreceptors, and this subcellular defect underpins the photopic vision loss in these patients (15, 18). To date, no other diseases or cellular defects have been reported in people lacking ATF6 function.

The absence of ATF6 has a notable impact across a number of organs in various organisms and experimental disease models. In the eyes, *Atf6*$^{-/-}$ mice exhibit late-onset retinal degeneration and accelerated degeneration when bred with the P23H rhodopsin model of retinitis pigmentosa (10, 19) . In the liver and pancreas, *Atf6*$^{-/-}$ mice and zebrafish with ATF6 morpholinos demonstrate symptoms like steatosis, fatty liver, beta-cell loss, obesity, and type 2 diabetes-like features after intraperitoneal tunicamycin injection (20, 21), high-fat diet (22), when bred with Agouti and Akita diabetes mouse models (22), or ethanol treatment (23). In the cardiovascular system, *Atf6*$^{-/-}$ mice show myocardial damage and reduced cardiac function in models of ischemic heart disease (24, 25), and increased brain infarction in stroke models (26). In muscle, *Atf6*$^{-/-}$ mice showed increased myofiber damage after treadmill exercise challenge (27). In the colon, *Atf6*$^{-/-}$ mice developed severe colitis following dextran sulfate sodium administration (28). In neurological contexts, *Atf6*$^{-/-}$ mice demonstrate increased neuronal cell death in models of Parkinson's disease (29) and glutamate excitotoxicity (30), as well as hypothalamic neuron defects impacting water balance and urine production (31). Interestingly, the loss of ATF6 has some beneficial effects: *Atf6*$^{-/-}$ mice resist paralysis and show reduced spinal cord inflammation in a model of multiple sclerosis (32). *Atf6*$^{-/-}$ mice also display no notable differences from controls in an osteoarthritis model (33). Notably, under normal laboratory growing conditions, *Atf6*$^{-/-}$ mice were viable and showed none of the above changes except for the retinal decline seen with advanced age (10, 20).

In light of the broad range of organs impacted by a loss of ATF6 in animal models, in this study, we investigated whether patients lacking functional ATF6 had additional diseases or phenotypes other than the previously reported vision loss. Unexpectedly, we found that progressive sensorineural hearing loss was a prominent complaint in our patient cohorts. Furthermore, we identified a previously unappreciated auditory defect in *Atf6*$^{-/-}$ mice that phenocopied the hearing loss found in patients. Then, we characterized the cellular and molecular defects in the ear underlying hearing loss in the *Atf6*$^{-/-}$ mice.

Results

Human *ATF6* mutations are associated with hearing loss

Hearing loss was a prominent complaint in multiple achromatopsia patients carrying ATF6 disease variants. Hearing loss was reported by 3 achromatopsia siblings homozygous for a c.970C>T ATF6 variant that introduced an arginine-to-cysteine conversion at position 324 (Figure 1A, II:1, II:2, and II:3). This missense mutation abrogated ATF6 transcriptional activity in fibroblasts cultured from these siblings when challenged with tunicamycin and thapsigargin (10, 11). In all three subjects, audiometry testing showed hearing defects most evident in high-frequency ranges that affected right and left ears equally (Figure 1A, audiograms from II:1 at age 52, II:2 at age 43, and II:3 at age 49). Otoacoustic emissions were absent in subject II:1 and II:2. Subject II:3 showed some response but only up to 3 KHz on the right and 2 KHz on the left, and unusually high response amplitude in the 5 KHz band on the left (10 dB SPL, Supplemental Figure 1). The results indicate loss of outer hair cells in the area from 3-5 kHz in the left ear. However, there was evidence of a narrow island of surviving hair cells around the 5 kHz region in the left ear, which the audiologist marked as an anomalous finding. Hearing was not tested at this frequency, so some function may have been missed.

Comparison of audiograms performed at different timepoints revealed a progressive worsening of the hearing loss affecting both ears (Figure 1B, left and right audiograms from subject II:1 performed at age 40 and age 52, Supplemental Figure 2A). Figure 1C shows bilateral audiograms from subject II:2 performed at age 39 and age 43, Supplemental Figure 2B). Figure 1D shows bilateral audiograms from subject II:3 performed at age 31 and age 49. Medical genetic testing of blood samples from these three subjects showed no pathogenic variants in a 356-gene hereditary hearing loss panel (Supplemental Table 1). Commercial gene testing of saliva from subject II:3 also revealed no known genetic basis for hearing loss (23andMe ancestry test). Hearing loss was also reported in another achromatopsia patient homozygous for a c.1699T>A

ATF6 variant that introduced a tyrosine-to-asparagine conversion at position 567 (Figure 1E, II:1). This missense mutation also abrogated ATF6 transcriptional activity in fibroblasts challenged with tunicamycin and thapsigargin in vitro (10, 11). Audiometry testing showed auditory defects affecting the right and left ears equally (Figure 1E, audiogram at age 14). Genetic testing for hereditary hearing loss in patient II:1 (Figure 1E) was not conducted, as consent for genetic testing was not obtained. Additionally, progressive audiometry assessments were not conducted for this patient. Nonetheless, audiometric findings in individuals with ATF6 variants linked to disease, coupled with the absence of mutations in known hereditary sensorineural genes in at least three of these cases, suggested that ATF6 may be causative for sensorineural hearing loss.

***Atf6*$^{-/-}$ mice exhibit hearing loss**

To further investigate ATF6's role in hearing, we analyzed auditory responses in *Atf6*$^{-/-}$ mice. These mice carry a premature stop codon in exon IV and produce no ATF6 protein similar to some ATF6 disease alleles found in ACHM patients (13, 20). *Atf6*$^{-/-}$ mice are viable and have normal growth and development but display functional changes in many experimental ER stress-linked disease paradigms (20, 24-29, 31). Their hearing has not been studied. We evaluated auditory brainstem responses (ABRs) to assess auditory function in the absence of ATF6. First, we measured auditory function at postnatal day (P) 14, (i.e., 2 weeks), shortly after the onset of hearing function (34). In 2-week-old mice raised under normal vivarium conditions, measurements of ABRs to pure tones showed no statistically significant changes in ABR thresholds (measured in decibels sound pressure level; dB SPL) at all tested frequencies (i.e., 8k, 12k, 16k, 24k, 28k, and 32k) in *Atf6*$^{+/+}$ versus *Atf6*$^{-/-}$ mice (Figure 2A). However, by 2 months, the ABR thresholds of *Atf6*$^{-/-}$ mice were statistically significantly higher than those of *Atf6*$^{+/+}$ mice at all tested frequencies (*Two-way ANOVA, ****$p \leq 0.0001$*), with the highest thresholds at 32 kHz (high-frequency stimuli, Figure 2B). No significant gender differences in ABR thresholds were found in both *Atf6*$^{-/-}$ and

Atf6$^{+/+}$ (*Two-way ANOVA, P > 0.05*) in the 2-month ABR tests (Figure 2C and D). These findings demonstrate that *Atf6*$^{-/-}$ mice have normal hearing at onset of hearing (i.e., 2-week-old) but develop an auditory defect by 2-months.

Our transgenic *Atf6*$^{-/-}$ (10, 19, 20) mice were maintained in the C57BL/6J (B6J) genetic background. The B6J strain carries the defective *Cdh23ahl* allele and develops age-related hearing loss beginning at ~3-6 months worsening over the next 12-15 months (34-38). We assessed auditory structure/function in *Atf6*$^{-/-}$ mice at 2 months age because experiments in older mice would be confounded by the inherent hearing loss in the B6J genetic background. Thus, our results suggest that the hearing loss in *Atf6*$^{-/-}$ mice is not due to B6J background because all the recordings were performed at 2-week-old and 2-month-old mice. Next, we investigated cellular and molecular defects responsible for hearing loss in the *Atf6*$^{-/-}$ mice.

Normal inner and outer ear anatomy and no inflammation in *Atf6*$^{-/-}$ mouse ears

Bacterial infections of the middle ear, otitis media, affect 80% of the human population and can lead to chronic infection, inflammation, scarring, and tissue damage in the middle ear, leading to hearing loss (39-46). To investigate if *Atf6*$^{-/-}$ mice had infection, inflammation, scarring, or tissue damage in the middle ear, we analyzed histologic sections of the ears prepared from 2-month-old *Atf6*$^{-/-}$ mice. Neither *Atf6*$^{+/+}$ nor *Atf6*$^{-/-}$ mice showed infectious or inflammatory exudate extending from the Eustachian tube (Figure 3A and B, *arrows*), and the middle ear (ME) was open, patent, and free of inflammatory cells in all mice (Figure 3A and B). Furthermore, no scarring or tissue damage was noted in the middle ears of *Atf6*$^{+/+}$ and *Atf6*$^{-/-}$ mice. These findings support that hearing loss in *Atf6*$^{-/-}$ does not arise from middle ear inflammation and structural destruction.

Next, we examined the anatomy of the cochlea within the inner ear in *Atf6*$^{-/-}$ mice. The cochlea converts sound into sensorineural impulses transmitted to the brain to provide auditory information. Damage to the cochlear epithelial or sensorineural tissues such as stria vascularis (SV), organ of Corti (OC), or spiral ganglion cells (SG) can cause hearing loss (47-51). On histologic sections of the cochlea prepared from 2-month-old *Atf6*$^{+/+}$ (Figure 3C) and *Atf6*$^{-/-}$ mice (Figure 3D), we found normal cochlear anatomy in *Atf6*$^{-/-}$ mice with intact SV and SG as in *Atf6*$^{+/+}$ mice. Consistent with the histologic appearance, quantification of the number of spiral ganglion cells/area (Figure 3E, *Welch's t-test,* $p = 0.99$) and the thickness of stria vascularis (Figure 3F, *Welch's t-test,* $p = 0.86$)* showed no statistically significant differences between *Atf6*$^{+/+}$ and *Atf6*$^{-/-}$ mice. Therefore, these results indicate that the hearing defect in *Atf6*$^{-/-}$ mice was unlikely to arise from damage to SG cells or atrophy of the SV in the cochlea. In these histologic preparations, the organ of Corti also appeared structurally normal in *Atf6*$^{-/-}$ with discernible inner and outer hair cells separated by a tunnel (Fig 3C and 3D), but stereocilia and other subcellular morphology of hair cells could not be resolved with this method.

***Atf6*$^{-/-}$ cochlea shows loss of hair cells and disorganized hair cell stereocilia**

Hair cells use stereocilia bundles at their apex to detect sound wave pressure changes in the endolymph (49). Damage to hair cell structures decreases hearing sensitivity because hair cells cannot regenerate in mice/people (52-55). To evaluate hair cells in detail, we prepared cochlear whole mounts from *Atf6*$^{-/-}$ mice (56). Immunofluorescence with a hair cell-specific marker, myosin VII (57-59) and a filamentous actin marker, phalloidin (59, 60) were used to evaluate the cellular arrangement and the stereocilia of hair cells in *Atf6*$^{+/+}$ and *Atf6*$^{-/-}$ mice (Figure 4). At 2 months, there was apparent cell loss and disrupted arrangement of outer hair cells in the basal region of the cochlea (Figure 4A and B, *Welch's t-test,* $p = 0.02$, Supplemental Figure 3), but no cell loss was found among the inner hair cells in the cochlea (Figure 4A and B, *Welch's t-test,* $p = 0.28$). By contrast to the outer hair cell loss in the cochlear base, the outer hair cells in the apical region appeared to be preserved (Supplemental Figure 4).

The proper orientation, projection, and alignment of mechanosensory stereocilia on the apical surfaces of hair cells are essential for hearing. Actin labeling of the stereocilia bundles revealed severe disorganization of these structures in *Atf6*$^{-/-}$ mice (Figure 4). In the basal cochlea, many stereocilia on inner hair cells were misaligned and extended in random directions (arrowheads, Figure 4C and D, *Welch's t-test, p = 0.002*) in *Atf6*$^{-/-}$ mice (*arrowheads*) compared to the *Atf6*$^{+/+}$ mice. In this region of the cochlea, surviving outer hair cells also showed disorganized stereocilia (Figure 4E, *arrows*) in *Atf6*$^{-/-}$ mice. By contrast to the stereocilia damage seen in inner hair cells and outer hair cells from the basal cochlear, the stereocilia of inner hair cells (Supplemental Figure 4A, B, C, and D) and outer hair cells (Supplemental Figure 4A, B, E) in the apical region appeared normal. Together, these data identify cellular defects that underpin the hearing loss in *Atf6*$^{-/-}$ mice at 2 months of age: 1. damage to stereocilia on hair cells and 2. reduction of outer hair cell number focally.

Functional pathway analysis identifies enrichment of ER Stress, channel activity, actin filament organization, and neuronal death pathways in *Atf6*$^{-/-}$ cochlea

To identify molecular defects in the cochlea arising from *Atf6* deletion, we analyzed bulk-RNA-seq transcriptomes from *Atf6*$^{-/-}$ and *Atf6*$^{+/+}$ mice cochleae. Based on a cutoff for background value at 0.1 FPKM (fragments per kilobase of exon per million mapped reads), 15,952 transcripts were expressed in *Atf6*$^{+/+}$ and *Atf6*$^{-/-}$ cochlea (Supplemental Table 2). *Atf6*$^{-/-}$ mice have slow progressive hearing loss (that resembles the progressive hearing loss reported by our patients carrying ATF6 disease alleles, Figures 1 and 2). Therefore, we adopted a low fold change ($FC > 0.05$) threshold while maintaining statistical significance in Log2(fold changes) between the two groups (Figure 5A, $p \leq 0.05$ and fold change >0.05) yielding 1,869 statistically significant differentially expressed genes, represented by green dots above the blue line.

To gain insight into the functions of the 1,869 genes differentially expressed between *Atf6*$^{+/+}$ and *Atf6*$^{-/-}$ cochlea, we performed gene ontology (GO) analysis (gProfiler (https://biit.cs.ut.ee/gprofiler/, last accessed October 12, 2022, Supplemental Table 3) (61). Changes in biological processes and molecular function terms (62) were assessed from differential expression of the differentially expressed gene sets (Figure 5B). GO biological processes analysis revealed that differentially expressed genes (DEGs) between the *Atf6*$^{+/+}$ and *Atf6*$^{-/-}$ cochlea were strongly associated with ER stress (GO:0034976, Response to endoplasmic reticulum stress; GO:1905897, regulation of response to endoplasmic reticulum stress; GO:0034620, cellular response to unfolded protein); cellular ion homeostasis (GO:0030003, cellular cation homeostasis), actin function (GO:0032970, regulation of actin filament-based process), and neuron death (GO:0070997, neuron death) (Figure 5B). GO Molecular Function pathway analysis revealed that DEGs were also strongly associated with actin binding (GO:0003779, actin binding), channel activity (GO:0005261, cation channel activity, GO:0005216, ion channel activity, GO:0022803, passive transmembrane transporter activity, GO:0015267, channel activity), and ubiquitin-specific protease binding (GO:1990381) (Figure 5B). Next, CytoScape (3.8.2; (63)) was used to generate an enrichment map of common cellular themes between the biological processes and molecular function GO terms enriched in the *Atf6*$^{-/-}$ cochlea (Figure 5C, Supplemental Figure 5). The enrichment map further highlighted that DEGs were associated with ER protein misfolding (endoplasmic reticulum unfolded and retrograde ER cytosol nodes), actin cytoskeleton filament, ion homeostasis (divalent cation homeostasis and ion cation transport nodes), and regulation neuron death (Figure 5C). Together, the functional pathway analysis of *Atf6*$^{-/-}$ at 2-month-old cochlea transcriptomes revealed notable enrichment of ER stress, channel activity, actin filament organization, and neuron death processes.

Induction of Unfolded Protein Response, ER-Associated Protein Degradation, and ER stress-induced Apoptosis pathways in *Atf6*$^{-/-}$ cochlea

ER stress was one of the most enriched processes in the *Atf6*$^{-/-}$ cochlea transcriptome (Figure 5). ER stress triggers many cellular programs including the UPR, ER-associated protein degradation, autophagy, lipid metabolism/synthesis, oxidative phosphorylation, and cell death (2, 64-68). We investigated if these ER stress-regulated programs were altered in *Atf6*$^{-/-}$ cochlea transcriptomic datasets. In mammals, the UPR is comprised of 3 distinct signal transduction pathways regulated by IRE1, ATF6, and PERK, that generate the XBP1s, ATF6's cytosolic domain (ATF6f), and ATF4 transcription factors upon ER stress(2). Target genes of XBP1s, ATF6f, and ATF4 have been extensively characterized in mammals (15, 20, 69-75). To examine if UPR was induced in the *Atf6*$^{-/-}$cochlea, we probed expression of a panel of 118-IRE1/XBP1s, ATF6, and PERK/ATF4-regulated- target genes (UPR-regulated genes, Supplemental Table 4). We found statistically significant upregulation of the overall UPR-regulated gene panel in *Atf6*$^{-/-}$ cochlea (Figure 6A, gray violin plot, **** $p \leq 0.0001$, *Two-tailed Wilcoxon Signed Rank Test*). Within the UPR-regulated 118 gene panel, 36 genes were statistically significantly altered between *Atf6*$^{-/-}$ vs *Atf6*$^{+/+}$ cochlear: *Sec61a1, Cars, Shmt2, Asns, Wfs1, Rpn1, Hyou1, Slc3a2, Sec23b, Dnajb9, Aars, Hspa13, Tmem50b, Sec24d, Vegfa, Herpud1, Slc2a6, Ficd, Txndc11, Cbx4, Slc1a4, Rbm10, Sec31a, Piga, Trib3, Atf4, Syvn1, Hsp90b1, Derl1, Cnnm2, Derl3, Pdia4, Nucb2, Nars, Arfgap3, and Lman1*, Figure 6B, Supplemental Figure 6, and Supplemental Table 4, **** $p \leq 0.0001$, *** $p \leq 0.001$, ** $p \leq 0.01$, * $p \leq 0.05$ measured from DESeq2 analysis, Supplemental Table 4). Interestingly, nearly all (32/36 genes) notably altered UPR genes were up-regulated in *Atf6*$^{-/-}$ cochlea, and the top 12 most strongly induced UPR genes were closely linked to the PERK-ATF4 pathway (70-72) (Figure 6B). By contrast, all 4 statistically significantly down-regulated genes in *Atf6*$^{-/-}$ cochlea (*Tmem50b, Slc2a6, Hsp90b1, and Derl3*) were linked to ATF6 pathway (Supplemental Figure 6 and Supplemental Table 4; (15, 20, 69). Thus, our findings provide evidence that UPR, especially the PERK arm, is notably activated by ER stress in *Atf6*$^{-/-}$ cochlea. Furthermore, Gene Set Enrichment Analysis (GSEA) also confirmed marked enrichment in related terms: Response to ER stress (FDR = 0.18) and cellular response to unfolded protein (FDR = 0.18) in *Atf6*$^{-/-}$ cochlea transcriptome (Supplemental Figure 7).

ER-associated protein degradation (ERAD) is another cellular mechanism triggered by ER stress (64, 67, 73, 76). In our GO analysis of the *Atf6*$^{-/-}$ cochlear transcriptome, we did not find statistically significant association of the GO ERAD term (GO:0036503), but we did observe a statistically significant association of a related GO term ubiquitin-specific protease binding (Figure

5). To investigate ERAD status in *Atf6*$^{-/-}$ cochlea in more detail, we queried expression levels of 91 genes in the ERAD pathway gene set (Supplemental Table 5). We saw a statistically significant increase in median expression of the ERAD panel in *Atf6*$^{-/-}$ versus *Atf6*$^{+/+}$ cochleae (Figure 6C, blue violin plot, * $p \leq 0.05$, *Two-tailed Wilcoxon Signed Rank Test*). Within the gene panel, 14 ERAD pathway genes (*Herpud1, H13, Ubqln2, Uggt1, Fbxo27, Rhbdd1, Selenos, Syvn1, Derl1, Usp19, Nccrp1, Derl3, Hsp90b1, Psmc6*) were statistically significantly different in *Atf6*$^{-/-}$ vs *Atf6*$^{+/+}$ and 10 of these 14 ERAD genes were up-regulated in *Atf6*$^{-/-}$ mice cochlear (Figure 6D, * $p \leq 0.05$, ** $p \leq 0.01$, **** $p \leq 0.0001$ measured from DESeq2 analysis, Supplemental Table 5). Thus, these results support that ERAD is another ER stress-regulated mechanism induced in *Atf6*$^{-/-}$ cochlea.

Excessive or chronic ER stress triggers cell death (77-79). We saw hair cell dropout in *Atf6*$^{-/-}$ cochlea (Figure 4), and our GO analysis also revealed that the DEGs are notably associated with a cell death term, neuron death, in *Atf6*$^{-/-}$ cochlea (Figure 5). To investigate in more detail if ER stress-related cell death was induced in *Atf6*$^{-/-}$ cochlea, we queried expression levels of the 61 genes comprising the GO term Intrinsic Apoptotic Response to Endoplasmic Reticulum Stress (GO:0070059) in *Atf6*$^{-/-}$ cochlea transcriptomes (Supplemental Table 6). We observed a statistically significant increase in the median expression of intrinsic apoptotic response to ER stress gene panel in *Atf6*$^{-/-}$ versus *Atf6*$^{+/+}$ cochleae (Figure 6E, green violin plot, * $p \leq 0.05$, *Two-tailed Wilcoxon Signed Rank Test*). Within the 61-gene ER stress apoptotic response panel, 6 genes (*Chac1, Trib3, Itpr1, Atf4, Qrich1, and Bcl2l1*) were statistically significantly changed in *Atf6*$^{-/-}$ vs *Atf6*$^{+/+}$ cochlea transcriptomes, and these were all up-regulated in *Atf6*$^{-/-}$ mice (Figure 6F, * $p \leq 0.05$, ** $p \leq 0.01$, *** $p \leq 0.001$ measured from DESeq2 analysis, Supplemental Table 6). Together, these results support that UPR, ERAD, and ER stress-induced cell death are notably induced in *Atf6*$^{-/-}$ cochlea transcriptome. By contrast, autophagy, oxidative stress, and lipid synthesis/metabolism were not statistically significantly altered in the *Atf6*$^{-/-}$ cochlear transcriptome (Supplemental Figure 8 and Supplemental Table 7).

DEG analysis identifies dysregulation of actin filament/stereocilia-related genes and channel-related genes in *Atf6*$^{-/-}$ cochlea

GO analysis of *Atf6*$^{-/-}$ cochlea transcriptomes also revealed a notable association with terms related to actin filament organization (Figure 5B and C). GSEA confirmed enrichment in related terms: actin filament bundle assembly (FDR = 0.11) and auditory receptor cell stereocilium organization (FDR = 0.14) in *Atf6*$^{-/-}$ cochlea transcriptome (Supplemental Figure 9). Hair cell stereocilia consist of bundles of highly crosslinked actin filaments (F-actin) (80), and hair cell stereocilia were extensively damaged in *Atf6*$^{-/-}$ mice hair cells (Figure 4). To investigate in more detail how the loss of *Atf6* in cochlea affected actin-rich stereocilia genes, we queried combined actin filament/stereocilia-related gene sets (actin filament gene set: GO:0007015; Stereocilia gene set (81, 82); (Figure 7A)(Supplemental Table 8). We found that the overall mean expression of the 401 actin filament/stereocilia related combined gene panel was statistically significantly increased in *Atf6*$^{-/-}$ cochlea transcriptomes (Figure 7A, violin plot, **** $p \leq 0.0001$, Two-tailed Wilcoxon Signed Rank test). Furthermore, analysis of 105 stereocilia-enriched genes within the 401 gene panel (81, 82) was statistically significantly increased in *Atf6*$^{-/-}$ cochlea transcriptomes (Supplemental Figure 10, *violin plot, *$p \leq 0.05$*, Two-tailed Wilcoxon Signed Rank test*), and (Supplemental Table 8) identified 13 stereocilia genes (*Ocm, Fscn1, Nf2, Pfn2, Capza2, Calm1, Gpx2, Tprn, Pdzd7, Actn4, Magi1, Calm2, and Actr3*) that were statistically significantly different between *Atf6*$^{-/-}$ and *Atf6*$^{+/+}$ (Figure 7B, *$p \leq 0.05$, ** $p \leq 0.01$, measured from DESeq2 analysis, Supplemental Table 8). Thus, our analysis showed dysregulated expression of actin filament/stereocilia-related genes in *Atf6*$^{-/-}$ cochlea that could correlate with or directly underlie the disorganization of hair cell bundles seen by microscopy.

Last, we investigated expression of ion channel-related genes in *Atf6*$^{-/-}$ vs *Atf6*$^{+/+}$ cochlea transcriptomes because GO analysis identified multiple channel terms enriched in *Atf6*$^{-/-}$ cochlea transcriptome (Figure 5B). We saw no changes in the mean expression levels of channel-related gene sets but did find statistically significant alterations of several individual genes encoding chloride channels (*Clic4 and Ano3*), potassium channels (*Kcnj14, Kcng4, Kcnj10, Kcnn2, Kcnd1, Kcnip4, Kcnn3, Kcnq5, Kcnd3, Kcnb2, Kcnh7*), and sodium channels (*Scn3b*) in *Atf6*$^{-/-}$ vs *Atf6*$^{+/+}$ cochleae (Figure 7C, * $p \leq 0.05$, ** $p \leq 0.01$, ** $p \leq 0.001$ **** $p \leq 0.0001$, Supplemental Table 9) (81). By contrast, calcium channel-related genes were not statistically significantly altered between *Atf6*$^{-/-}$ and *Atf6*$^{+/+}$ in cochlea transcriptomes (e.g., *Cacnb1, Cacnb2, and Cacnb3*). Taken together, a subset of these ion channel genes also showed dysregulation (both up- and down-expression) in *Atf6*$^{-/-}$ cochlea.

Discussion

ATF6 controls a key signal transduction pathway of the UPR that helps cells adapt to ER stress. In people, cone photoreceptors require ATF6 for development and function, and loss of ATF6 leads to congenital vision loss diseases like achromatopsia (10, 13, 15, 68). Here, we report that hair cells in the organ of Corti also require ATF6 for function and viability, and loss of ATF6 leads to a second human disease – sensorineural hearing loss-which is phenocopied in *Atf6*$^{-/-}$ mice. Cochleae from these mice show extensive damage to hair cell stereocilia and focal hair cell loss. Transcriptional analysis of cochleae from *Atf6*$^{-/-}$ mice reveals a marked induction of the UPR transcriptional program, especially through the PERK arm. These current findings, coupled with our previous studies, indicate that ATF6 inactivation causes a vision and hearing loss syndrome in people arising from cone photoreceptor and hair cell dysfunction. Furthermore, at the molecular level, hair cell damage and hearing loss arising from the loss of ATF6 are linked to ER stress and UPR activation in the cochlea.

We visualized hair cell damage in cochleae in 2-month-old *Atf6*$^{-/-}$ mice with hearing loss (Figures 2 and 4), and the patient audiometric testing results support that human hair cells are also defective when ATF6 function is lost. Otoacoustic emissions, which are sounds generated by healthy outer hair cells in the cochlea (83, 84), were absent in two patients. Despite detailed clinical evaluations, one patient showed limited responses at 3 kHz in the right ear and 2 kHz in the left ear. A heightened response at 5 kHz in the left ear likely resulted from reduced olivocochlear suppression, causing increased cochlear gain (85). The results indicate that there is loss of outer hair cells in the ATF6 patient. Furthermore, audiograms in these patients showed downward slopes at high frequencies (Figure 1), a pattern typically linked to outer hair cell defects (86, 87). Similar to the quality of the auditory recording defects found in patients, the 2-month-old *Atf6*$^{-/-}$ mice also showed statistically significantly higher ABR thresholds at high-frequency stimuli (32-kHz) compared to lower-frequency stimuli (Figure 2B). Thus, these clinical auditory phenotypes support a common pathogenic mechanism causing hearing loss in humans and mice with loss of ATF6 function. Disease-associated ATF6 variants found in people disrupt transcriptional signaling via distinct pathomechanisms (11). Further investigation of audiograms from patients across a broader range of ATF6 variants is needed to determine ATF6's role in sensorineural hearing loss and whether auditory phenotypic differences are seen between ATF6 genotypes.

The 2-month-old *Atf6*$^{-/-}$ mice showed markedly increased ABR thresholds at all frequencies tested (Figure 2) that correspond, anatomically, with apical (low frequency) to basal (high frequency) increasing cochlea pathology. *Atf6*$^{-/-}$ mice showed stereocilia disorganization of inner and outer hair cells in the basal cochlea, with hair cell loss limited to OHCs in this region (Figure 4). Prior mouse experiments have demonstrated that the basal cochleae in mice was most susceptible to noise and ototoxic drugs (88-90). Hu et al. (2016) found OHC death starts in the basal turns and spreads apically in Cdh23erl/erl cochleae(88). Ikaheimo et al. (2021) reported stereocilia fusion and synapse degradation in basal OHCs and IHCs of Manf-deficient mice (91). Fujinami et al. (2012) showed that ER stress impairs high-frequency hearing in tunicamycin-treated rats due to basal OHC damage (92). Jongkamonwiwat et al. (2020) revealed that high-frequency regions are prone to noise-induced stereocilia damage (59). Based on these findings, we propose that *Atf6* deficiency confers susceptibility to ER stress throughout the cochlea. According to this model, the genetic vulnerability to ER stress, compounded with natural environmental ER stressors encountered by the cochlea during life, causes outer hair cells begin to dropout in the basal region. Then, hair cell loss spreads to the rest of the cochlea accounting for the deterioration of hearing in ATF6 patients and mice.

What are possible mechanisms that make hair cells vulnerable to the loss of ATF6? Hair cells require numerous membrane and structural proteins to maintain the stereocilia's “hair-like” structure, essential for sound detection. Without ATF6, stereocilia may disintegrate as their necessary proteins are not produced in sufficient quantity or quality. Similarly, we previously found that photoreceptors, which also have polarized cilia-derived structures (the photoreceptor outer segments), are highly sensitive to ATF6 loss (10, 12, 93). These findings suggest that ATF6 is crucial for the development, stability, and function of polarized sensory neurons.

Another mechanism that could explain hair cell vulnerability to ATF6 loss relates to hair cells' susceptibility to noise-induced proteotoxicity. Excessive noise disrupts proteostasis in hair cells and is a primary cause of progressive hearing loss in people (59). Proteomic and transcriptional analyses of noise-exposed mouse cochlea show increased chaperone and degradation activity, as well as activation of the UPR and ERAD to combat noise-induced protein damage (59). In addition to noise, ER stress-inducing chemicals or aging can also lead to ER stress and hearing loss in animal and in vitro cell assays (92, 94-98). These findings highlight noise as a major cause of cochlear ER stress and help explain why ATF6 is essential for preserving cochlear health and hearing.

Highlighting the importance of protein quality control to cochlear health, sensorineural hearing loss is a frequent phenotype when ER quality control genes are mutated. Similar to *Atf6*$^{-/-}$ mice, mice lacking the ER quality control regulator, *Mesencephalic astrocyte-derived neurotrophic factor* (*MANF*), show hair cell stereocilia disarray, progressive outer hair cell death, elevated ABR thresholds, and UPR induction in the cochlea (89, 91). Clinical audiograms from a patient with a homozygous loss-of-function *MANF* variant also revealed severe bilateral sensorineural hearing loss that progressively worsened with age (91). However, early-onset juvenile diabetes arises with the loss of MANF in mice and patients (99) but not in *Atf6*$^{-/-}$ mice and has not been reported in patients carrying ATF6 loss-of-function variants. In people, disease variants of *Wolfram Syndrome 1* (*WFS1*), another ER quality control component, cause autosomal recessive sensorineural hearing loss (100), and mice homozygous for exon 8 deletion or an E864K missense change of WFS1 also develop hearing defects (101). WFS1-associated deafness is also linked with diabetes insipidus, diabetes mellitus, and retinal ganglion cell-related optic nerve atrophy in people as part of the clinical symptoms of DIDMOAD/Wolfram Syndrome

(102, 103). In mice, genetic inactivation of *Transmembrane and tetratricopeptide Repeat 4/ Transmembrane O-Mannosyltransferase Targeting Cadherins 4* (*Tmtc4*), another ER quality control regulator, also triggers hearing loss, hair cell death, and UPR activation (104), reminiscent of the defects observed in *Atf6*$^{-/-}$ mice. These studies support that proteostasis genes and mechanisms are critical for cochlea health and function.

Our current study shows that ATF6 is essential for hearing, and our prior studies showed that ATF6 was essential for vision in people (10, 13, 15, 68). This combination of auditory and visual dysfunction, along with the biallelic inheritance of *ATF6* variants, mirrors Usher syndrome, characterized by blindness, deafness, and autosomal recessive inheritance (105). Many mouse models of Usher syndrome recapitulate the auditory defects found in patients but show little to no vision defects (105), *Atf6*$^{-}$/$^{-}$ mice also exhibit hearing loss (Figures 1, 2, 4) but retain normal vision until 18 months of age, when a gradual decline in photopic and scotopic responses occurs (10, 19). At the subcellular level, Usher syndrome genes and ATF6 share no obvious mechanistic functions. Many Usher syndrome proteins are structural components of stereocilia in hair cells and ciliary/peri-ciliary/calyceal processes in photoreceptor, while ATF6 is an ER membrane-bound transcription factor that regulates ER protein folding fidelity. Therefore, we propose that Atf6 inactivation causes a syndrome in patients with phenotypic (blindness-deafness) and cellular (photoreceptor-hair cell) features that resemble Usher syndrome, combined with molecular pathomechanisms (ER stress, UPR dysregulation) that are causal in Wolfram syndrome.

Sensorineural hearing loss is one of the most common sensory disorders affecting approximately 466 million people worldwide (https://www.who.int/news-room/fact-sheets/detail/deafness-and-hearing-loss). Small molecules that modulate protein quality control offer promising therapeutic strategies for protecting against sensorineural hearing loss by maintaining cochlear protein quality (88, 89, 91, 92, 94-98, 104, 106). For example, the chemical chaperones taurine-conjugated derivative of ursodeoxycholic acid (TUDCA), preserved hair cells and delayed hearing loss in *erl* mice (107). Small molecule inhibition of the PERK arm of the UPR and Integrated Stress Response (ISR) using ISRIB protected hair cells and attenuated hearing loss in the *Tmtc4*$^{-/-}$ mouse (104), and in a noise-induced rodent model of hearing loss (108). Beyond PERK, our study suggests that targeting the ATF6 and IRE1 arms of the UPR may also benefit cochlear health. Human and mouse genetic data indicate that ATF6 inactivation contributes to hearing loss, making small molecule ATF6 activators a potential therapy. AA147, which enhances ATF6 activity, was effective in restoring ATF6 function in retinal organoids from patients with ATF6 disease variants (15, 109). In addition, the XBP1s transcription factor, generated by the IRE1 arm of the UPR, shares many gene targets with ATF6 (15, 76, 110). Therefore, small molecule IRE1-XBP1s activators may also have otoprotective properties. Conversely, small molecule ATF6 inhibitors (e.g., CeapinA7) and IRE1-XBP1 inhibitors may show ototoxic side effects. Our study highlights both the ototoxic effects of ER stress dysregulation and the potential for drugs to mitigate ER stress-related ototoxicity.

Materials and Methods

Sex as a biological variable

All studies included a minimum of two animals per sex per group, and no sex-specific effects were found.

Human subjects

The CRHO91 and CHRO649 patients underwent comprehensive otologic and audiometric evaluations through their healthcare providers. Otoscopy revealed no external ear abnormalities in all patients. Audiometric examinations, conducted by registered audiologists, measured air conduction pure-tone hearing thresholds at 0.25, 0.5, 1, 2, 3, 4, 6, and 8 kHz in each ear.

Animals

Transgenic *Atf6*$^{+/+}$ and *Atf6*$^{-/-}$ (10, 19, 20) on a pure C57BL/6J (B6J) background were used, originally developed by Dr. Randal Kaufman (Sanford Burnham Prebys Medical Discovery Institute, La Jolla, CA, USA) and maintained in our laboratory (Stanford University, Stanford, CA, USA). The B6J strain has been extensively used as a model for early onset age-related hearing loss (34-37). B6J mice show high-frequency hearing loss initiating at 3-6 months of age, which then progresses in severity and spreads to lower frequencies with advancing age over the next 12 to 15 months(38). All experiments used female or male *Atf6*$^{-/-}$ mice and control *Atf6*$^{+/+}$ littermates, at postnatal (P) days 14 (i.e., 2-week, n=8 *Atf6*$^{+/+}$; n=8 *Atf6*$^{-/-}$) and P60 (i.e., 2-month, n=10 *Atf6*$^{+/+}$; n=6 *Atf6*$^{-/-}$). For all experiments, animals were kept in cyclic 12-hour light/dark conditions with free access to food and water.

Auditory brainstem response

The detailed protocols for auditory brainstem response (ABR) acquisition in mice were performed as previously published (111). All acquisitions were performed in a sound-attenuating chamber

(Sonora Technology Co., Kanagawa, Japan). Prior to input in the chamber, mice were anaesthetized using a combination of ketamine (40 mg/kg; KETASET, Fort Dodge, IA, USA) and xylazine (8 mg/kg, X-Ject SA; Butler, Dublin, OH, USA) using similar procedures as our published protocols (111). Following deep anesthesia, the animals were maintained on a warming pad, and three needle electrodes (recording, reference, and ground) were inserted subcutaneously. Tone pips (3 ms duration, frequencies at 8, 12, 16, 24, 28 and 32 kilohertz (kHz) and intensities at 20, 40, 60, or 80 dB SPL (decibel sound pressure level) were delivered to the left ears at a rate of 19 times per second through a calibrated earphone (Stax Ltd., Saitama, Japan). ABR signals were recorded using BioSigRP software on a Tucker Davis Technology System 3 recording rig (Tucker-Davis Technologies, Alachua, FL, USA), and 512 recordings were averaged for each animal in each condition. Following ABR testing, the same cohort of mice underwent comprehensive histological examination of both the middle and inner ear tissues.

Tissue preparation

Mice were anesthetized using a combination of ketamine (40 mg/kg; KETASET, Fort Dodge, IA, USA) and xylazine (8 mg/kg, X-Ject SA; Butler, Dublin, OH, USA) at P14 and P60. Inner and middle ears were dissected and fixed in 4% paraformaldehyde overnight at 4°C. Inner and middle ears were later decalcified in 0.5M ethylenediaminetetraacetic acid (EDTA), pH 7.5, overnight at 4°C (Merck, Rahway, NJ, USA) or until clear and later placed in 30% sucrose for cryoprotection at 4°C until fully sunken. After decalcification, cochleae were mounted in optimal cutting temperature (OCT) compound for cryostat sectioning. Cochlear sections of 10 μm thickness were collected with a Leica CM1950 cryostat (Leica Biosystems Inc., Buffalo Grove, IL, USA) and placed on Superfrost Plus slides (Fisher Scientific, Waltham, MA, USA). For whole mount, the organ of Corti was microdissected as previously described (56).

Hematoxylin and Eosin Staining

Cochlear sections (10µm) were collected on gelatin-coated slides for hematoxylin and eosin staining. Slides were dipped in Harris hematoxylin for 1 minute then they were washed in tap water and dehydrated in alcohol. Slides were then dipped in Eosin-Phloxyine for 30 seconds, then dehydrated in a series of 95% ethanol and 100% ethanol followed by 5 minutes in xylene and mounted in xylene-based mounting medium (Vector Laboratories, Burlingame, CA, USA). ImageJ software version 1.50i (National Institutes of Health, Bethesda, MD, USA; http://imagej.nih.gov/ij/) was used to measure the thickness of stria vascularis (SV). For each section, three measurements of the SV thickness were taken at each section, spaced approximately 50 µm apart, which were then averaged for each section. SV thickness measurements were collected from six cochleae from separate animals for 2-month *Atf6*$^{+/+}$ *Atf6*$^{-/-}$ mice. In addition, the number of spiral ganglion (SG) cells in both *Atf6*$^{+/+}$ and *Atf6*$^{-/-}$ were manually counted at 2-month (n=6).

Cochlear Whole Mounts and Immunohistochemistry

For whole mount immunohistochemistry, cochleas were fixed in 4% PFA overnight at 4°C and then decalcified with 0.5M EDTA, overnight at 4 °C. The organ of Corti was microdissected as above. Whole mounts were washed with PBS and then incubated with 0.05% Triton in 10% normal donkey serum (NDS) for 1 hour at room temperature. Whole mounts were then incubated overnight at 4°C with rabbit anti-myosin VI primary antibody (Cat # 25-6790, Proteus Biosciences, Ramona, CA, USA) at a dilution of 1:300 in PBS. The whole mounts were then washed with PBS and incubated for 4 hours at room temperature with a secondary antibody donkey anti-rabbit IgG AlexaFlour488 (Cat # A-21206, 1:300 dilution, Thermo Fisher Scientific, Carlsbad, CA, USA) and Texas Red-X-conjugated Phalloidin (Cat # T7471, 1,400 dilution, Thermo Fisher Scientific, Carlsbad, CA, USA). Whole mounts were again washed with PBS and mounted with Vectashield Antifade Mounting Media (Cat # H-1000-10, Vector Laboratories, Newark, CA, USA). Images were collected with a Leica SP8 confocal microscope with lightning deconvolution and processed using LasX Image Analysis software at the UCSD, School of Medicine Microscopy Core.

RNA-Seq analysis

RNA-Seq analysis was performed as previously described (15). Whole cochlea of mice were collected and RNA extraction was performed following manufacturer's instructions (Cat # 74104, Qiagen RNAeasy Mini kit, Qiagen, Germantown, MD, USA). RNA-sequencing was performed by BGI's Eukaryotic Strand-specific Transcriptome Resequencing service (BGI, Shenzhen, China; http://biosys.bgi.com), using the proprietary DNBSEQ stranded mRNA library and providing paired-end 100 bp reads at 30 million reads per sample. Alignment of the sequencing data was performed using the HISAT2 alignment program (v2.0.4) to the (Mus_musculus_GCF_000001635.27_GRCm39). Gene expression and normalized reads (in FPKM) were determined by RSEM software (v1.2.18) (112). The DESeq2 package (v1.4.5) (113) was used to determine the differential expression between control and experimental groups and calculate the statistical significance of our findings.

Functional Enrichment Analysis

gProfiler (University of Tartu, Tartu, Estonia; https://biit.cs.ut.ee/gprofiler/) was used for functional enrichment analysis. Gene ontology (GO) analysis was used for functional annotation and pathway analysis (molecular functions, Biological Processes) (114). From the RNA-Seq experiments, gene expression with statistically different Log2 (fold change) expression ($p \leq 0.05$, greater than 0.1FPKM) and a fold change greater than 0.05 between *Atf6*$^{+/+}$ and *Atf6*$^{-/-}$ cochleae were used as the input. In our study, the *Atf6*$^{-/-}$ mice have slow progressive hearing loss (that resembles the progressive hearing loss reported by our patients carrying ATF6 disease alleles). Therefore, we adopted a low fold change (FC>0.05) threshold but still maintaining statistically significant p-value <0.05 in defining 1869 DEGs for pathway analysis out of the original 15,000+

genes identified with differential expression between mutant and wild-type.

These 1869 DEGs used in our study identified enrichment of ER stress pathways in *Atf6*$^{-/-}$ cochlear. This finding is compatible with previous studies of other cell types and tissues in *Atf6*$^{-/-}$ mice that also found ER stress dysregulation (8, 19, 21, 22, 115) and supports the physiologic relevance of the DEGs used in our study.

The gene enrichment map file, containing enriched terms from all databases, produced by gProfiler was imported into Cytoscape (version 3.8.2, Institute for Systems Biology, Seattle, WA, USA) and visualization of all terms into enrichment map was done by Cytoscape plug-in, Enrichment Map (116). Terms were grouped together into clusters by another Cytoscape plug-in, clusterMaker2. The created clusters were labeled by Cytoscape plug-in, Auto Annotate (117, 118). Alternatively, Gene Set Enrichment Analysis (GSEA) software (Broad Institute, Cambridge, MA, USA; https://www.broadinstitute.org/gsea/) was used to perform functional enrichment analysis. Pre-ranked lists were entered with the same gene sets and ranked based on expression values relative to wildtype controls. Weighted analysis with the GO reference database was performed, and GSEA enrichment plots were presented.

Statistics

All data were expressed as mean ± standard error of the mean (SEM). Statistical significance was defined as a *p*-value less than 0.05, with annotations as follows: _*p ≤ 0.05, **p ≤ 0.01, ***p ≤ 0.001, and ****p ≤ 0.0001._ All statistics were calculated using GraphPad Prism 9 (GraphPad Software, San Diego, CA, USA). Two-way ANOVA was used to compare average ABR thresholds at five frequency regions (8, 12, 16, 24, 28, and 32 kHz) between *Atf6*$^{+/+}$ and *Atf6*$^{-/-}$ mice (Figure 2). To evaluate whether the thickness of stria vascularis and number of spiral ganglion cell/area differed between *Atf6*$^{+/+}$ and *Atf6*$^{-/-}$ cochleae, measurements were quantified by ImageJ software version 1.53 (NIH, Bethesda, MD, USA, last accessed March 15, 2022). Welch's t-test was used to examine the difference between two different means (Figure 3E and F). To evaluate whether the number of hair cells (i.e., outer hair cells and inner hair cells) and number disorganized bundles of stereocilia in inner hair cells differed between *Atf6*$^{+/+}$ and *Atf6*$^{-/-}$ cochleae, *Welch's t-test* was used to examine the difference between two different means (Figure 4B and D). Violin plots comparing *Atf6*$^{+/+}$ and *Atf6*$^{-/-}$ transcriptomes were generated using the Log2 fold change data from the differential expression analysis for UPR-related genes, ERAD genes, Intrinsic apoptotic response to ER-related genes, and actin filaments/stereocilia-related genes. Differences in expression of gene sets were evaluated for statistical significance using *two-tailed Wilcoxon Signed Rank* Test (Figure 6A, C, and E, Figure 7A). For analyses of RNA-seq data, statistical significance was calculated for differences in expression of UPR-related genes, ERAD genes, Intrinsic apoptotic response to ER-related genes, stereocilia-related genes, chloride channel genes, potassium channel genes, and sodium channel gene, and was reported as *P* value for *n* = 6 *Atf6*$^{-/-}$ and n = 5 *Atf6*$^{+/+}$ independent cochleae calculated by DESeq2 analysis (Figure 6B, D, and F, Figure 7B and C; Supplemental Table 2).

Study Approval

All mouse procedures were approved by the Institutional Animal Care and Use Committee. ACHM human subjects provided written informed consent, approved by local ethical review boards, following the Declaration of Helsinki.

Data Availability

RNA-seq data are available at the NCBI Gene Expression Omnibus (GSE242321). All other data are provided within the article and/or in the Supporting Data Values file.

Author Contributions:

E-J.L. and J.H.L. designed all the experiments and interpreted the results. J.H.L. provided ethical oversight and secured funding. Experimental contributions were made by E-J.L., K.K., L.A.S., and E.C. RNA sequencing and analysis were performed by E-J.L., K.K., M.S.D., H.M., and G.Z. Data and statistical analysis were contributed by E-J.L., K.K., G.Z., and M.S.D. Clinical data collection was carried out by K.J.S. and J.H.L. The manuscript was written by E-J.L. and J.H.L. All authors, including A.F.R., contributed to reviewing and editing the manuscript.

Acknowledgements

The authors thank the ATF6 patients and families who inspired this study. This research was supported by NIH grants P30EY026877, R01EY027735; R01AG046495; R01NS125674; R01NS088485; CIRM DISC2-10973; and VA Merits I01BX002284 I01BX001205.

References

1. Haze K, Yoshida H, Yanagi H, Yura T, and Mori K. Mammalian transcription factor ATF6 is synthesized as a transmembrane protein and activated by proteolysis in response to endoplasmic reticulum stress. *Mol Biol Cell.* 1999;10(11):3787-99.
2. Walter P, and Ron D. The unfolded protein response: from stress pathway to homeostatic regulation. *Science.* 2011;334(6059):1081-6.
3. Nadanaka S, Yoshida H, and Mori K. Reduction of disulfide bridges in the lumenal domain of ATF6 in response to glucose starvation. *Cell Struct Funct.* 2006;31(2):127-34.
4. Ye J, Rawson RB, Komuro R, Chen X, Davé UP, Prywes R, et al. ER stress induces cleavage of membrane-bound ATF6 by the same proteases that process SREBPs. *Mol Cell.* 2000;6(6):1355-64.
5. Shen J, Snapp EL, Lippincott-Schwartz J, and Prywes R. Stable binding of ATF6 to BiP in the endoplasmic reticulum stress response. *Mol Cell Biol.* 2005;25(3):921-32.
6. Wang Y, Shen J, Arenzana N, Tirasophon W, Kaufman RJ, and Prywes R. Activation of ATF6 and an ATF6 DNA binding site by the endoplasmic reticulum stress response. *J Biol Chem.* 2000;275(35):27013-20.
7. Wu J, Rutkowski DT, Dubois M, Swathirajan J, Saunders T, Wang J, et al. ATF6alpha optimizes long-term endoplasmic reticulum function to protect cells from chronic stress. *Dev Cell.* 2007;13(3):351-64.
8. Yamamoto K, Sato T, Matsui T, Sato M, Okada T, Yoshida H, et al. Transcriptional induction of mammalian ER quality control proteins is mediated by single or combined action of ATF6alpha and XBP1. *Dev Cell.* 2007;13(3):365-76.
9. Wang M, and Kaufman RJ. Protein misfolding in the endoplasmic reticulum as a conduit to human disease. *Nature.* 2016;529(7586):326-35.

10. Kohl S, Zobor D, Chiang WC, Weisschuh N, Staller J, Gonzalez Menendez I, et al. Mutations in the unfolded protein response regulator ATF6 cause the cone dysfunction disorder achromatopsia. *Nat Genet.* 2015;47(7):757-65.

11. Chiang WC, Chan P, Wissinger B, Vincent A, Skorczyk-Werner A, Krawczyński MR, et al. Achromatopsia mutations target sequential steps of ATF6 activation. *Proc Natl Acad Sci U S A.* 2017;114(2):400-5.

12. Skorczyk-Werner A, Chiang WC, Wawrocka A, Wicher K, Jarmuż-Szymczak M, Kostrzewska-Poczekaj M, et al. Autosomal recessive cone-rod dystrophy can be caused by mutations in the ATF6 gene. *Eur J Hum Genet.* 2017;25(11):1210-6.

13. Lee EJ, Chiang WJ, Kroeger H, Bi CX, Chao DL, Skowronska-Krawczyk D, et al. Multiexon deletion alleles of ATF6 linked to achromatopsia. *JCI Insight.* 2020;5(7).

14. Kroeger H, Grimsey N, Paxman R, Chiang WC, Plate L, Jones Y, et al. The unfolded protein response regulator ATF6 promotes mesodermal differentiation. *Sci Signal.* 2018;11(517).

15. Kroeger H, Grandjean JMD, Chiang WJ, Bindels DD, Mastey R, Okalova J, et al. ATF6 is essential for human cone photoreceptor development. *Proc Natl Acad Sci U S A.* 2021;118(39).

16. Ansar M, Santos-Cortez RL, Saqib MA, Zulfiqar F, Lee K, Ashraf NM, et al. Mutation of ATF6 causes autosomal recessive achromatopsia. *Hum Genet.* 2015;134(9):941-50.

17. Xu M, Gelowani V, Eblimit A, Wang F, Young MP, Sawyer BL, et al. ATF6 Is Mutated in Early Onset Photoreceptor Degeneration With Macular Involvement. *Invest Ophthalmol Vis Sci.* 2015;56(6):3889-95.

18. Mastey RR, Georgiou M, Langlo CS, Kalitzeos A, Patterson EJ, Kane T, et al. Characterization of Retinal Structure in ATF6-Associated Achromatopsia. *Invest Ophthalmol Vis Sci.* 2019;60(7):2631-40.

19. Lee EJ, Chan P, Chea L, Kim K, Kaufman RJ, and Lin JH. ATF6 is required for efficient rhodopsin clearance and retinal homeostasis in the P23H rho retinitis pigmentosa mouse model. *Sci Rep.* 2021;11(1):16356.

20. Wu J, Rutkowski DT, Dubois M, Swathirajan J, Saunders T, Wang J, et al. ATF6alpha optimizes long-term endoplasmic reticulum function to protect cells from chronic stress. *Dev Cell.* 2007;13(3):351-64.

21. Yamamoto K, Takahara K, Oyadomari S, Okada T, Sato T, Harada A, et al. Induction of liver steatosis and lipid droplet formation in ATF6alpha-knockout mice burdened with pharmacological endoplasmic reticulum stress. *Mol Biol Cell.* 2010;21(17):2975-86.

22. Usui M, Yamaguchi S, Tanji Y, Tominaga R, Ishigaki Y, Fukumoto M, et al. Atf6α-null mice are glucose intolerant due to pancreatic β-cell failure on a high-fat diet but partially resistant to diet-induced insulin resistance. *Metabolism.* 2012;61(8):1118-28.

23. Howarth DL, Lindtner C, Vacaru AM, Sachidanandam R, Tsedensodnom O, Vasilkova T, et al. Activating transcription factor 6 is necessary and sufficient for alcoholic fatty liver disease in zebrafish. *PLoS Genet.* 2014;10(5):e1004335.

24. Jin JK, Blackwood EA, Azizi K, Thuerauf DJ, Fahem AG, Hofmann C, et al. ATF6 Decreases Myocardial Ischemia/Reperfusion Damage and Links ER Stress and Oxidative Stress Signaling Pathways in the Heart. *Circ Res.* 2017;120(5):862-75.

25. Blackwood EA, Azizi K, Thuerauf DJ, Paxman RJ, Plate L, Kelly JW, et al. Pharmacologic ATF6 activation confers global protection in widespread disease models by reprograming cellular proteostasis. *Nat Commun.* 2019;10(1):187.

26. Yoshikawa A, Kamide T, Hashida K, Ta HM, Inahata Y, Takarada-Iemata M, et al. Deletion of Atf6α impairs astroglial activation and enhances neuronal death following brain ischemia in mice. *J Neurochem.* 2015;132(3):342-53.

27. Wu J, Ruas JL, Estall JL, Rasbach KA, Choi JH, Ye L, et al. The unfolded protein response mediates adaptation to exercise in skeletal muscle through a PGC-1α/ATF6α complex. *Cell Metab.* 2011;13(2):160-9.

28. Cao J, Dai DL, Yao L, Yu HH, Ning B, Zhang Q, et al. Saturated fatty acid induction of endoplasmic reticulum stress and apoptosis in human liver cells via the PERK/ATF4/CHOP signaling pathway. *Mol Cell Biochem.* 2012;364(1-2):115-29.

29. Egawa N, Yamamoto K, Inoue H, Hikawa R, Nishi K, Mori K, et al. The endoplasmic reticulum stress sensor, ATF6α, protects against neurotoxin-induced dopaminergic neuronal death. *J Biol Chem.* 2011;286(10):7947-57.

30. Kezuka D, Tkarada-Iemata M, Hattori T, Mori K, Takahashi R, Kitao Y, et al. Deletion of Atf6α enhances kainate-induced neuronal death in mice. *Neurochem Int.* 2016;92:67-74.

31. Azuma Y, Hagiwara D, Lu W, Morishita Y, Suga H, Goto M, et al. Activating transcription factor 6α is required for the vasopressin neuron system to maintain water balance under dehydration in male mice. *Endocrinology.* 2014;155(12):4905-14.

32. Ta HM, Le TM, Ishii H, Takarada-Iemata M, Hattori T, Hashida K, et al. Atf6α deficiency suppresses microglial activation and ameliorates pathology of experimental autoimmune encephalomyelitis. *J Neurochem.* 2016;139(6):1124-37.

33. Kung LHW, Mullan L, Soul J, Wang P, Mori K, Bateman JF, et al. Cartilage endoplasmic reticulum stress may influence the onset but not the progression of experimental osteoarthritis. *Arthritis Res Ther.* 2019;21(1):206.

34. Mikaelian DO. Development and degeneration of hearing in the C57/b16 mouse: relation of electrophysiologic responses from the round window and cochlear nucleus to cochlear anatomy and behavioral responses. *Laryngoscope.* 1979;89(1):1-15.

35. Henry KR, and Chole RA. Genotypic differences in behavioral, physiological and anatomical expressions of age-related hearing loss in the laboratory mouse. *Audiology.* 1980;19(5):369-83.

36. Hequembourg S, and Liberman MC. Spiral ligament pathology: a major aspect of age-related cochlear degeneration in C57BL/6 mice. *J Assoc Res Otolaryngol.* 2001;2(2):118-29.

37. Wang J, Menchenton T, Yin S, Yu Z, Bance M, Morris DP, et al. Over-expression of X-linked inhibitor of apoptosis protein slows presbycusis in C57BL/6J mice. *Neurobiol Aging.* 2010;31(7):1238-49.

38. Kane KL, Longo-Guess CM, Gagnon LH, Ding D, Salvi RJ, and Johnson KR. Genetic background effects on age-related hearing loss associated with Cdh23 variants in mice. *Hear Res.* 2012;283(1-2):80-8.

39. Bluestone CD, and Doyle WJ. Anatomy and physiology of eustachian tube and middle ear related to otitis media. *J Allergy Clin Immunol.* 1988;81(5 Pt 2):997-1003.

40. Alsarraf R, Jung CJ, Perkins J, Crowley C, Alsarraf NW, and Gates GA. Measuring the indirect and direct costs of acute otitis media. *Arch Otolaryngol Head Neck Surg.* 1999;125(1):12-8.

41. Graydon K, Waterworth C, Miller H, and Gunasekera H. Global burden of hearing impairment and ear disease. *J Laryngol Otol.* 2019;133(1):18-25.

42. Tong S, Amand C, Kieffer A, and Kyaw MH. Trends in healthcare utilization and costs associated with acute otitis media in the United States during 2008-2014. *BMC Health Serv Res.* 2018;18(1):318.

43. Dewan KK, Sedney C, Caulfield AD, Su Y, Ma L, Blas-Machado U, et al. Probing Immune-Mediated Clearance of Acute Middle Ear Infection in Mice. *Front Cell Infect Microbiol.* 2021;11:815627.

44. Monasta L, Ronfani L, Marchetti F, Montico M, Vecchi Brumatti L, Bavcar A, et al. Burden of disease caused by otitis media: systematic review and global estimates. *PLoS One.* 2012;7(4):e36226.

45. Vos B, Noll D, Pigeon M, Bagatto M, and Fitzpatrick EM. Risk factors for hearing loss in children: a systematic literature review and meta-analysis protocol. *Syst Rev.* 2019;8(1):172.

46. DeAntonio R, Yarzabal JP, Cruz JP, Schmidt JE, and Kleijnen J. Epidemiology of otitis media in children from developing countries: A systematic review. *Int J Pediatr Otorhinolaryngol.* 2016;85:65-74.

47. Dallos P, Wu X, Cheatham MA, Gao J, Zheng J, Anderson CT, et al. Prestin-based outer hair cell motility is necessary for mammalian cochlear amplification. *Neuron.* 2008;58(3):333-9.

48. Yu WM, and Goodrich LV. Morphological and physiological development of auditory synapses. *Hear Res.* 2014;311:3-16.

49. Fettiplace R. Hair Cell Transduction, Tuning, and Synaptic Transmission in the Mammalian Cochlea. *Compr Physiol.* 2017;7(4):1197-227.

50. Liberman MC, and Kujawa SG. Cochlear synaptopathy in acquired sensorineural hearing loss: Manifestations and mechanisms. *Hear Res.* 2017;349:138-47.

51. Ó Maoiléidigh D, and Ricci AJ. A Bundle of Mechanisms: Inner-Ear Hair-Cell Mechanotransduction. *Trends in neurosciences.* 2019;42(3):221-36.

52. Kawamoto K, Izumikawa M, Beyer LA, Atkin GM, and Raphael Y. Spontaneous hair cell regeneration in the mouse utricle following gentamicin ototoxicity. *Hear Res.* 2009;247(1):17-26.

53. Burns JC, Cox BC, Thiede BR, Zuo J, and Corwin JT. In vivo proliferative regeneration of balance hair cells in newborn mice. *J Neurosci.* 2012;32(19):6570-7.

54. Golub JS, Tong L, Ngyuen TB, Hume CR, Palmiter RD, Rubel EW, et al. Hair cell replacement in adult mouse utricles after targeted ablation of hair cells with diphtheria toxin. *J Neurosci.* 2012;32(43):15093-105.

55. Wagner EL, and Shin JB. Mechanisms of Hair Cell Damage and Repair. *Trends in neurosciences.* 2019;42(6):414-24.

56. Montgomery SC, and Cox BC. Whole Mount Dissection and Immunofluorescence of the Adult Mouse Cochlea. *J Vis Exp.* 2016(107).

57. Hasson T, Heintzelman MB, Santos-Sacchi J, Corey DP, and Mooseker MS. Expression in cochlea and retina of myosin VIIa, the gene product defective in Usher syndrome type 1B. *Proc Natl Acad Sci U S A.* 1995;92(21):9815-9.

58. Soni LE, Warren CM, Bucci C, Orten DJ, and Hasson T. The unconventional myosin-VIIa associates with lysosomes. *Cell Motil Cytoskeleton.* 2005;62(1):13-26.

59. Jongkamonwiwat N, Ramirez MA, Edassery S, Wong ACY, Yu J, Abbott T, et al. Noise Exposures Causing Hearing Loss Generate Proteotoxic Stress and Activate the Proteostasis Network. *Cell Rep.* 2020;33(8):108431.

60. Faulstich H, Zobeley S, Rinnerthaler G, and Small JV. Fluorescent phallotoxins as probes for filamentous actin. *J Muscle Res Cell Motil.* 1988;9(5):370-83.

61. Raudvere U, Kolberg L, Kuzmin I, Arak T, Adler P, Peterson H, et al. g:Profiler: a web server for functional enrichment analysis and conversions of gene lists (2019 update). *Nucleic Acids Res.* 2019;47(W1):W191-W8.

62. Ashburner M, Ball CA, Blake JA, Botstein D, Butler H, Cherry JM, et al. Gene ontology: tool for the unification of biology. The Gene Ontology Consortium. *Nat Genet.* 2000;25(1):25-9.

63. Cline MS, Smoot M, Cerami E, Kuchinsky A, Landys N, Workman C, et al. Integration of biological networks and gene expression data using Cytoscape. *Nat Protoc.* 2007;2(10):2366-82.

64. Meusser B, Hirsch C, Jarosch E, and Sommer T. ERAD: the long road to destruction. *Nat Cell Biol.* 2005;7(8):766-72.

65. Rowland AA, and Voeltz GK. Endoplasmic reticulum-mitochondria contacts: function of the junction. *Nat Rev Mol Cell Biol.* 2012;13(10):607-25.

66. Wu H, Carvalho P, and Voeltz GK. Here, there, and everywhere: The importance of ER membrane contact sites. *Science.* 2018;361(6401).

67. Mehrtash AB, and Hochstrasser M. Ubiquitin-dependent protein degradation at the endoplasmic reticulum and nuclear envelope. *Semin Cell Dev Biol.* 2019;93:111-24.

68. Lee EJ, Diaz-Aguilar MS, Min H, Choi J, Valdez Duran DA, Grandjean JM, et al. Mitochondria and Endoplasmic Reticulum Stress in Retinal Organoids from Patients with Vision Loss. *Am J Pathol.* 2022.

69. Bommiasamy H, Back SH, Fagone P, Lee K, Meshinchi S, Vink E, et al. ATF6alpha induces XBP1-independent expansion of the endoplasmic reticulum. *J Cell Sci.* 2009;122(Pt 10):1626-36.

70. Han J, Back SH, Hur J, Lin YH, Gildersleeve R, Shan J, et al. ER-stress-induced transcriptional regulation increases protein synthesis leading to cell death. *Nat Cell Biol.* 2013;15(5):481-90.

71. Harding HP, Zhang Y, Zeng H, Novoa I, Lu PD, Calfon M, et al. An integrated stress response regulates amino acid metabolism and resistance to oxidative stress. *Mol Cell.* 2003;11(3):619-33.

72. Lu PD, Jousse C, Marciniak SJ, Zhang Y, Novoa I, Scheuner D, et al. Cytoprotection by pre-emptive conditional phosphorylation of translation initiation factor 2. *EMBO J.* 2004;23(1):169-79.

73. Lee AH, Iwakoshi NN, and Glimcher LH. XBP-1 regulates a subset of endoplasmic reticulum resident chaperone genes in the unfolded protein response. *Mol Cell Biol.* 2003;23(21):7448-59.

74. Sriburi R, Bommiasamy H, Buldak GL, Robbins GR, Frank M, Jackowski S, et al. Coordinate regulation of phospholipid biosynthesis and secretory pathway gene

expression in XBP-1(S)-induced endoplasmic reticulum biogenesis. *J Biol Chem.* 2007;282(10):7024-34.

75. Shaffer AL, Shapiro-Shelef M, Iwakoshi NN, Lee AH, Qian SB, Zhao H, et al. XBP1, downstream of Blimp-1, expands the secretory apparatus and other organelles, and increases protein synthesis in plasma cell differentiation. *Immunity.* 2004;21(1):81-93.

76. Shoulders MD, Ryno LM, Genereux JC, Moresco JJ, Tu PG, Wu C, et al. Stress-independent activation of XBP1s and/or ATF6 reveals three functionally diverse ER proteostasis environments. *Cell Rep.* 2013;3(4):1279-92.

77. Rao RV, Poksay KS, Castro-Obregon S, Schilling B, Row RH, del Rio G, et al. Molecular components of a cell death pathway activated by endoplasmic reticulum stress. *J Biol Chem.* 2004;279(1):177-87.

78. Lin JH, Li H, Yasumura D, Cohen HR, Zhang C, Panning B, et al. IRE1 signaling affects cell fate during the unfolded protein response. *Science.* 2007;318(5852):944-9.

79. Sano R, and Reed JC. ER stress-induced cell death mechanisms. *Biochim Biophys Acta.* 2013;1833(12):3460-70.

80. Flock A, and Cheung HC. Actin filaments in sensory hairs of inner ear receptor cells. *J Cell Biol.* 1977;75(2 Pt 1):339-43.

81. Tang F, Chen X, Jia L, Li H, Li J, and Yuan W. Differential Gene Expression Patterns Between Apical and Basal Inner Hair Cells Revealed by RNA-Seq. *Front Mol Neurosci.* 2019;12:332.

82. Liu H, Giffen KP, Chen L, Henderson HJ, Cao TA, Kozeny GA, et al. Molecular and cytological profiling of biological aging of mouse cochlear inner and outer hair cells. *Cell Rep.* 2022;39(2):110665.

83. Kemp DT. Stimulated acoustic emissions from within the human auditory system. *J Acoust Soc Am.* 1978;64(5):1386-91.

84. Baiduc RR, Lee J, and Dhar S. Spontaneous otoacoustic emissions, threshold microstructure, and psychophysical tuning over a wide frequency range in humans. *J Acoust Soc Am.* 2014;135(1):300-14.

85. Miranda FA, and Aguilar-Vidal E. Magnitude of the contralateral efferent olivocochlear effect as a function of the frequency. *J Otol.* 2022;17(2):67-71.

86. Demeester K, van Wieringen A, Hendrickx JJ, Topsakal V, Huyghe J, Fransen E, et al. Heritability of audiometric shape parameters and familial aggregation of presbycusis in an elderly Flemish population. *Hear Res.* 2010;265(1-2):1-10.

87. Vaden KI, Matthews LJ, Eckert MA, and Dubno JR. Longitudinal Changes in Audiometric Phenotypes of Age-Related Hearing Loss. *J Assoc Res Otolaryngol.* 2017;18(2):371-85.

88. Hu J, Li B, Apisa L, Yu H, Entenman S, Xu M, et al. ER stress inhibitor attenuates hearing loss and hair cell death in Cdh23. *Cell Death Dis.* 2016;7(11):e2485.

89. Herranen A, Ikäheimo K, Lankinen T, Pakarinen E, Fritzsch B, Saarma M, et al. Deficiency of the ER-stress-regulator MANF triggers progressive outer hair cell death and hearing loss. *Cell Death Dis.* 2020;11(2):100.

90. Johnson KR, Zheng QY, and Noben-Trauth K. Strain background effects and genetic modifiers of hearing in mice. *Brain Res.* 2006;1091(1):79-88.

91. Ikäheimo K, Herranen A, Iivanainen V, Lankinen T, Aarnisalo AA, Sivonen V, et al. MANF supports the inner hair cell synapse and the outer hair cell stereocilia bundle in the cochlea. *Life Sci Alliance.* 2022;5(2).

92. Fujinami Y, Mutai H, Mizutari K, Nakagawa S, and Matsunaga T. A novel animal model of hearing loss caused by acute endoplasmic reticulum stress in the cochlea. *J Pharmacol Sci.* 2012;118(3):363-72.

93. Kroeger H, Grandjean JMD, Chiang W-CJ, Bindels DD, Mastey R, Okalova J, et al. ATF6 is essential for human cone photoreceptor development. *Proceedings of the National Academy of Sciences.* 2021;118(39):e2103196118.

94. Oishi N, Duscha S, Boukari H, Meyer M, Xie J, Wei G, et al. XBP1 mitigates aminoglycoside-induced endoplasmic reticulum stress and neuronal cell death. *Cell Death Dis.* 2015;6(5):e1763.

95. Kishino A, Hayashi K, Hidai C, Masuda T, Nomura Y, and Oshima T. XBP1-FoxO1 interaction regulates ER stress-induced autophagy in auditory cells. *Sci Rep.* 2017;7(1):4442.

96. Xue Q, Li C, Chen J, Guo H, Li D, and Wu X. The Protective effect of the endoplasmic reticulum stress-related factors BiP/GRP78 and CHOP/Gadd153 on noise-induced hearing loss in guinea pigs. *Noise Health.* 2016;18(84):247-55.

97. Tu Y, Fan G, Sun H, Cai X, and Kong W. Endoplasmic reticulum stress is involved in spiral ganglion neuron apoptosis following chronic kanamycin-induced deafness. *Biosci Rep.* 2019;39(2).

98. Wang W, Sun Y, Chen S, Zhou X, Wu X, and Kong W. Impaired unfolded protein response in the degeneration of cochlea cells in a mouse model of age-related hearing loss. *Exp Gerontol.* 2015;70:61-70.

99. Montaser H, Patel KA, Balboa D, Ibrahim H, Lithovius V, Näätänen A, et al. Loss of MANF Causes Childhood-Onset Syndromic Diabetes Due to Increased Endoplasmic Reticulum Stress. *Diabetes.* 2021;70(4):1006-18.

100. Karzon R, Narayanan A, Chen L, Lieu JEC, and Hershey T. Longitudinal hearing loss in Wolfram syndrome. *Orphanet J Rare Dis.* 2018;13(1):102.

101. Richard EM, Brun E, Korchagina J, Crouzier L, Affortit C, Alves S, et al. Wfs1. *Cell Death Dis.* 2023;14(6):387.

102. Strom TM, Hörtnagel K, Hofmann S, Gekeler F, Scharfe C, Rabl W, et al. Diabetes insipidus, diabetes mellitus, optic atrophy and deafness (DIDMOAD) caused by mutations in a novel gene (wolframin) coding for a predicted transmembrane protein. *Hum Mol Genet.* 1998;7(13):2021-8.

103. Inoue H, Tanizawa Y, Wasson J, Behn P, Kalidas K, Bernal-Mizrachi E, et al. A gene encoding a transmembrane protein is mutated in patients with diabetes mellitus and optic atrophy (Wolfram syndrome). *Nat Genet.* 1998;20(2):143-8.

104. Li J, Akil O, Rouse SL, McLaughlin CW, Matthews IR, Lustig LR, et al. Deletion of Tmtc4 activates the unfolded protein response and causes postnatal hearing loss. *J Clin Invest.* 2018;128(11):5150-62.

105. Williams DS. Usher syndrome: animal models, retinal function of Usher proteins, and prospects for gene therapy. *Vision Res.* 2008;48(3):433-41.

106. Xia K, Ma H, Xiong H, Pan Q, Huang L, Wang D, et al. Trafficking abnormality and ER stress underlie functional deficiency of hearing impairment-associated connexin-31 mutants. *Protein Cell.* 2010;1(10):935-43.

107. Hu J, Xu M, Yuan J, Li B, Entenman S, Yu H, et al. Tauroursodeoxycholic acid prevents hearing loss and hair cell death in Cdh23(erl/erl) mice. *Neuroscience.* 2016;316:311-20.

108. Rouse SL, Matthews IR, Li J, Sherr EH, and Chan DK. Integrated stress response inhibition provides sex-dependent protection against noise-induced cochlear synaptopathy. *Sci Rep.* 2020;10(1):18063.

109. Paxman R, Plate L, Blackwood EA, Glembotski C, Powers ET, Wiseman RL, et al. Pharmacologic ATF6 activating compounds are metabolically activated to selectively modify endoplasmic reticulum proteins. *Elife.* 2018;7.

110. Plate L, Cooley CB, Chen JJ, Paxman RJ, Gallagher CM, Madoux F, et al. Small molecule proteostasis regulators that reprogram the ER to reduce extracellular protein aggregation. *Elife.* 2016;5.

111. Cederholm JM, Froud KE, Wong AC, Ko M, Ryan AF, and Housley GD. Differential actions of isoflurane and ketamine-based anaesthetics on cochlear function in the mouse. *Hear Res.* 2012;292(1-2):71-9.

112. Li B, and Dewey CN. RSEM: accurate transcript quantification from RNA-Seq data with or without a reference genome. *BMC Bioinformatics.* 2011;12:323.

113. Love MI, Huber W, and Anders S. Moderated estimation of fold change and dispersion for RNA-seq data with DESeq2. *Genome Biol.* 2014;15(12):550.

114. Reimand J, Isserlin R, Voisin V, Kucera M, Tannus-Lopes C, Rostamianfar A, et al. Pathway enrichment analysis and visualization of omics data using g:Profiler, GSEA, Cytoscape and EnrichmentMap. *Nat Protoc.* 2019;14(2):482-517.

115. Wu J, Rutkowski DT, Dubois M, Swathirajan J, Saunders T, Wang J, et al. ATF6α Optimizes Long-Term Endoplasmic Reticulum Function to Protect Cells from Chronic Stress. *Developmental Cell.* 2007;13(3):351-64.

116. Shannon P, Markiel A, Ozier O, Baliga NS, Wang JT, Ramage D, et al. Cytoscape: a software environment for integrated models of biomolecular interaction networks. *Genome Res.* 2003;13(11):2498-504.

117. Liberzon A, Subramanian A, Pinchback R, Thorvaldsdóttir H, Tamayo P, and Mesirov JP. Molecular signatures database (MSigDB) 3.0. *Bioinformatics.* 2011;27(12):1739-40.

118. Subramanian A, Tamayo P, Mootha VK, Mukherjee S, Ebert BL, Gillette MA, et al. Gene set enrichment analysis: a knowledge-based approach for interpreting genome-wide expression profiles. *Proc Natl Acad Sci U S A.* 2005;102(43):15545-50.

Figures and Figure legends

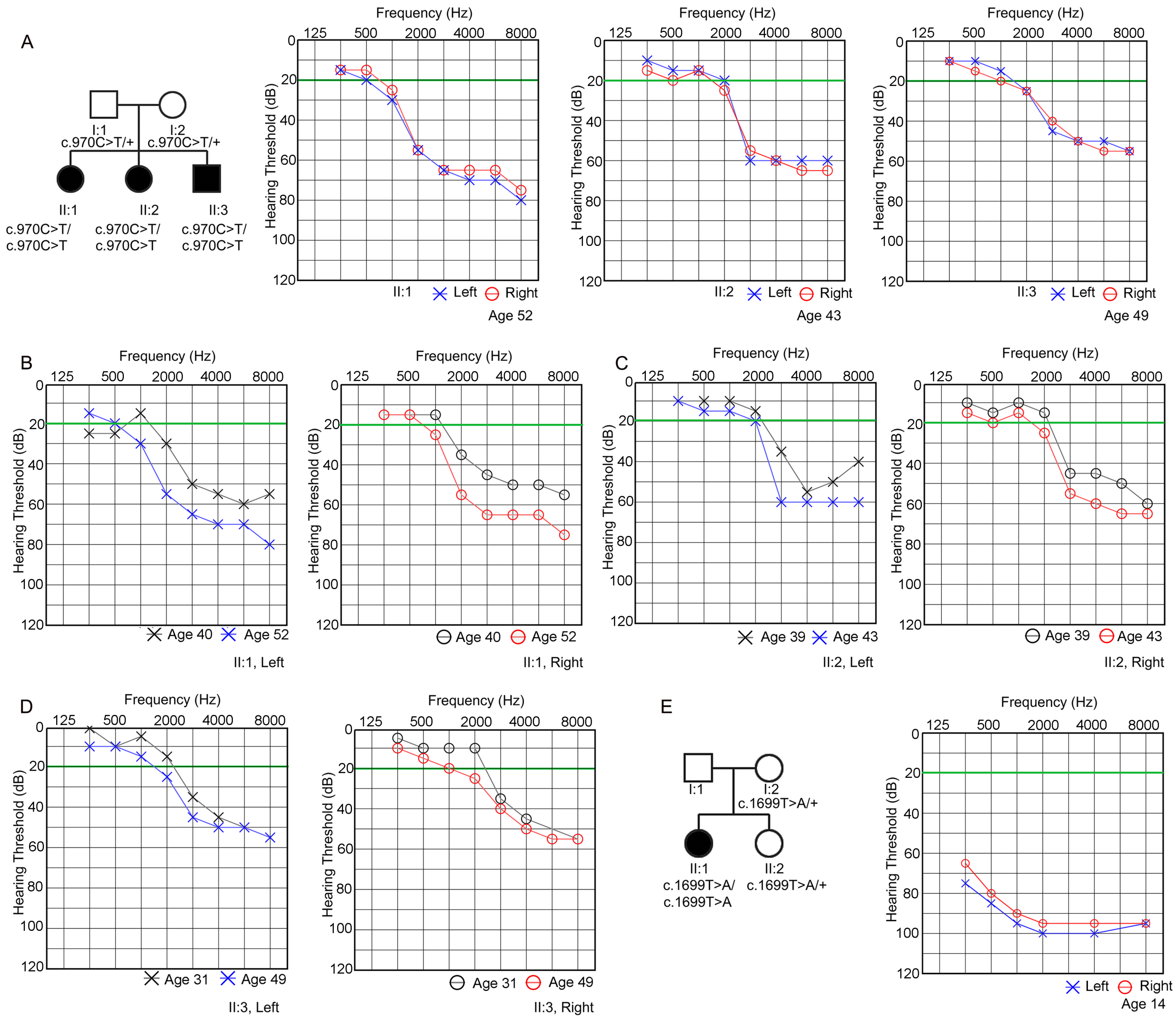

Figure 1. Human *ATF6* mutations are linked to hearing loss. (A) Pedigree of family carrying the point mutation (c.970C>T, p.Arg324Cys) and audiograms from individuals aged 52, 43, and 49 showing moderate high-frequency hearing loss in both right (red line) and left (blue line) ears. (B) Audiograms from patient II:1 at ages 40 and 52 reveal progressive high-frequency hearing loss. (C) Audiograms from patient II:2 at ages 39 and 43 show similar progression. (D) Audiograms from patient II:3 at ages 31 and 49 show some progression of high-frequency hearing loss. (E)

Pedigree of family carrying with the point mutation (c.1699T>A, p.Tyr567Asn, Age 14) shows severe low- to high-frequency hearing loss in both right (red line) and left (blue line) ears. Green line indicates normal hearing threshold. dB, decibel; Hz, hertz.

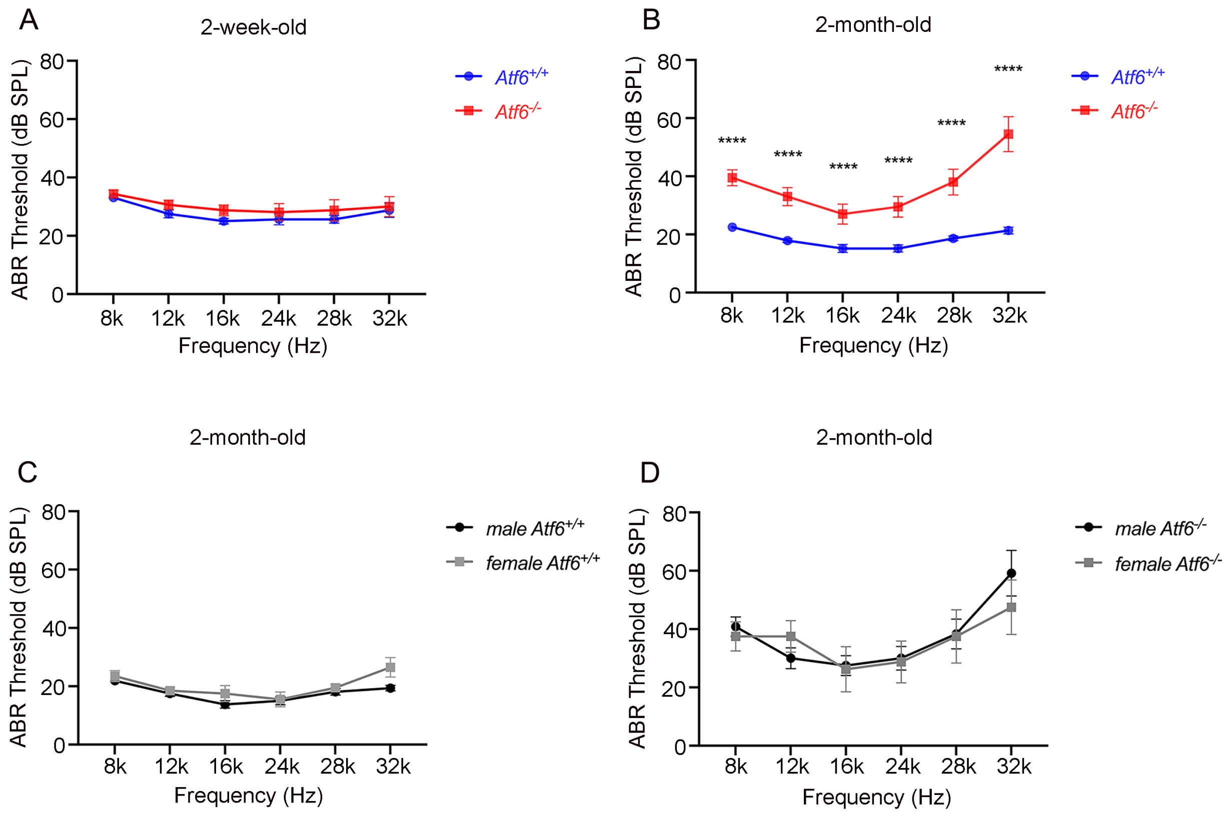

Figure 2. Hearing loss in *Atf6*$^{-/-}$ mice. (A) At postnatal day 14 (2-week-old), auditory brainstem response (ABR) thresholds at six frequencies were indistinguishable between *Atf6*$^{+/+}$ (n = 8, blue line) and *Atf6*$^{-/-}$ (n = 8, red line) mice (mean ± SEM, *Two-way ANOVA, p >0.05*). (B) At 2 months, *Atf6*$^{-/-}$ mice (n = 10, red line) showed statistically significantly increased ABR thresholds (consistent with profound hearing loss) at all frequencies compared to *Atf6*$^{+/+}$ (n=13, blue line, mean ± SEM, *Two-way ANOVA, ****p ≤ 0 .0001*). (C, D) No gender differences in ABR thresholds between 2-month-old female (gray line) and male (black line) *Atf6*$^{+/+}$ (n = 8, male; n = 5 female) and *Atf6*$^{-/-}$ (n = 6, male; n = 4 female) mice (mean ± SEM, *Two-way ANOVA, P >0.05*). dB SPL, decibels sound pressure level; kHZ, kilohertz.

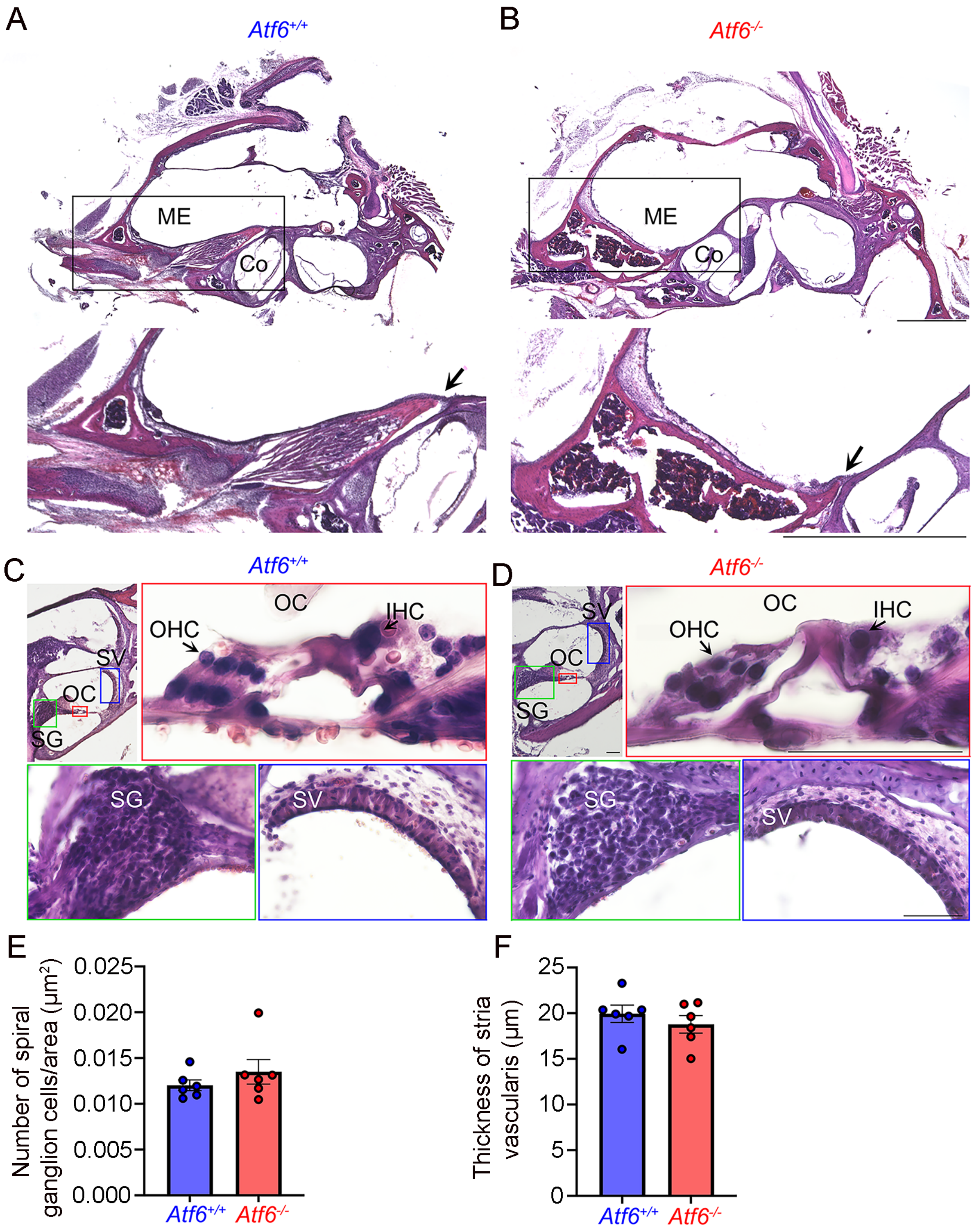

Figure 3. Histology of *Atf6*$^{+/+}$ and *Atf6*$^{-/-}$ middle and inner ear. (A, B) Light micrographs taken from cryostat sections and processed for Hematoxylin & Eosin (H&E) staining of middle ear (ME), of

2-month-old *Atf6*$^{+/+}$ and *Atf6*$^{-/-}$ mice, show normal anatomy and no infection in the middle ear. The bottom image represents higher magnification of the boxed region of the middle ear and shows no accumulation of inflammatory exudate extending from the Eustachian tube (*arrows*) or in the middle ear cavity. (C, D) Histologic sections of 2-month-old organ of corti (OC, red box), derived from *Atf6*$^{+/+}$ and *Atf6*$^{-/-}$ mice, show no disrupted anatomic architecture of the *Atf6*$^{-/-}$ cochlea (Co) as well as intact Stria vascularis (SV, blue box), Spiral Ganglia (SG, green box), Outer Hair Cells (OHC), and Inner Hair Cells (IHC). (E) The number of spiral ganglion cell/area and (F) the thickness of the stria vascularis were not statistically significantly different between *Atf6*$^{+/+}$ (n = 6) and *Atf6*$^{-/-}$ cochlea (n = 6). Dots represent individual measurements. Data represent mean ± SEM, *Welch's t-test,* $p > 0.05$. ME, Middle Ear; Co, cochlea; SG, spiral ganglion; SV, stria vascularis; OC, organ of corti; OHC, outer hair cell; IHC, inner hair cell. Scale bar, 1 mm (A and B); 1 mm (A and B, inset); 50 um (C and D).

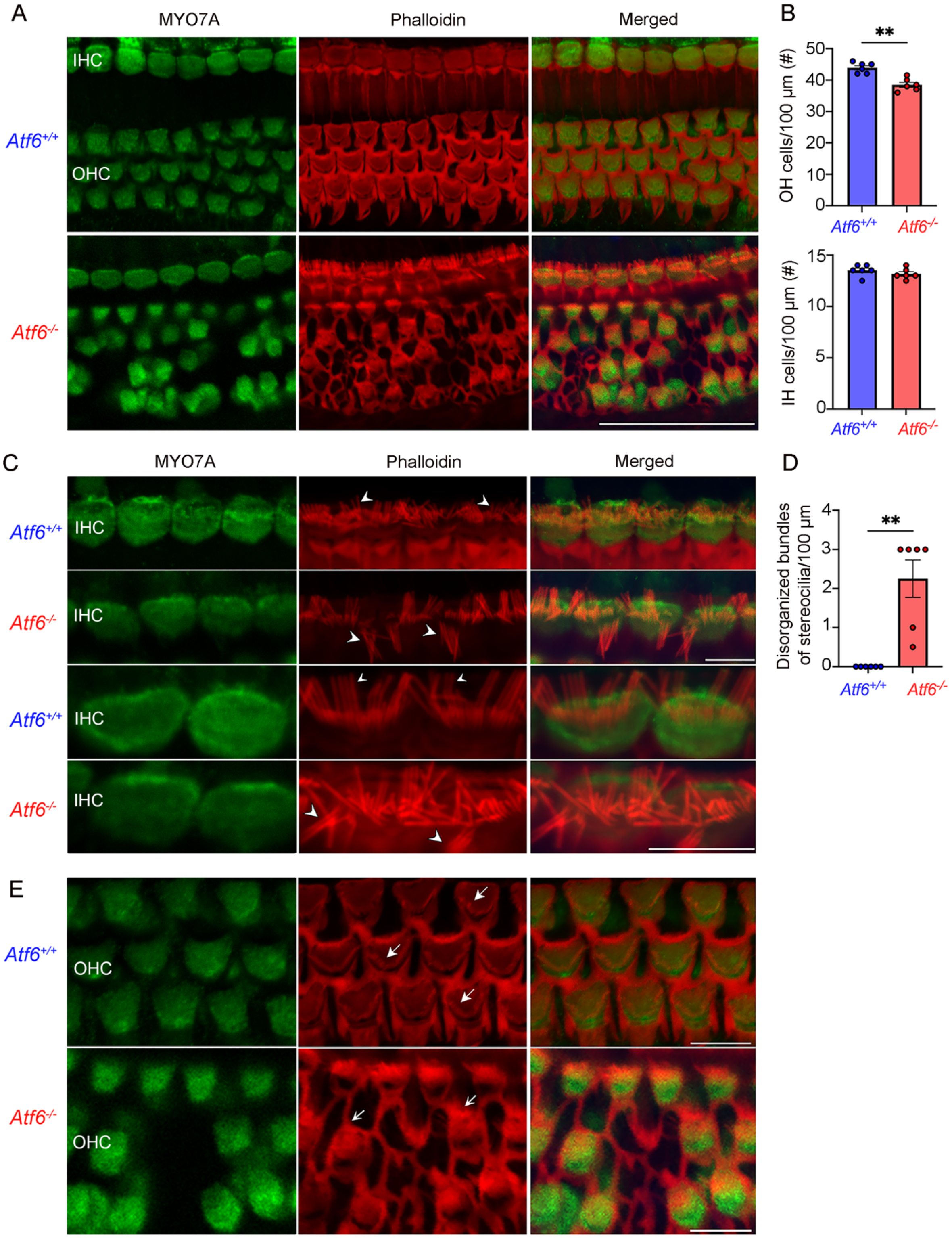
A
MYO7A
Phalloidin
Merged
Atf6+/+
IHC
OHC
Atf6-/-
B
**
OH cells/100 µm (#)
50
40
30
20
10
0
Atf6+/+
Atf6-/-
IH cells/100 µm (#)
15
10
5
0
Atf6+/+
Atf6-/-
C
MYO7A
Phalloidin
Merged
Atf6+/+
IHC
Atf6-/-
IHC
Atf6+/+
IHC
Atf6-/-
IHC
D
Disorganized bundles of stereocilia/100 µm
4
3
2
1
0
**
Atf6+/+
Atf6-/-
E
Atf6+/+
OHC
Atf6-/-
OHC

Figure 4. Cochlear hair cells of *Atf6*$^{-/-}$ mice degenerate and exhibit disorganized stereocilia in the basal region (Approximate frequency 28-32kHz). *Atf6*$^{+/+}$ and *Atf6*$^{-/-}$ cochleae were stained for myosin 7a (MYO7A) and phalloidin to visualize hair cells and stereocilia, respectively. (A) Immunofluorescent confocal images of 2-month-old *Atf6*$^{-/-}$ outer hair cell show disorganized arrangement and loss of outer hair cells. (B) Histogram showing the number of OHCs and IHCs in 2-month-old *Atf6*$^{+/+}$ (n = 6) and *Atf6*$^{-/-}$ (n=6) cochlea. Counts refer to the number of hair cells encountered within the average of two separate 100 um linear extensions. (Each dot represents the average of two individual measurements; Data represents mean ± SEM, *Welch's t-test,* **$p \le 0.01$). (C) *Atf6*$^{+/+}$ mice maintain organized stereocilia on IHCs while *Atf6*$^{-/-}$ mice show IHC stereocilia abnormalities such as disorganized bundling (arrowheads) at 2-months of age. Bottom two rows are higher power images showing stereocilia organization in *Atf6*$^{+/+}$ vs *Atf6*$^{-/-}$ IHCs. (D) Quantitative analysis of disorganized IHC bundle reveals statistically significant disorganization stereocilia in 2-month-old *Atf6*$^{-/-}$ mice. Dots represent individual measurements (n=6). Data represent mean ± SEM, *Welch's t-test,* ** $p \le 0.01$. (E) Images of MYO7A- and phalloidin- stained *Atf6*$^{+/+}$ and *Atf6*$^{-/-}$ organ of Corti focusing on the stereocilia of the OHCs. In *Atf6*$^{-/-}$ mice (n=6), OHC stereocilia show severe changes in morphology when compared to OHC stereocilia from *Atf6*$^{+/+}$ mice (arrows, n=6). OHC, outer hair cell; IHC, inner hair cell. Scale bar, 50 um (A); 10um (C, E).

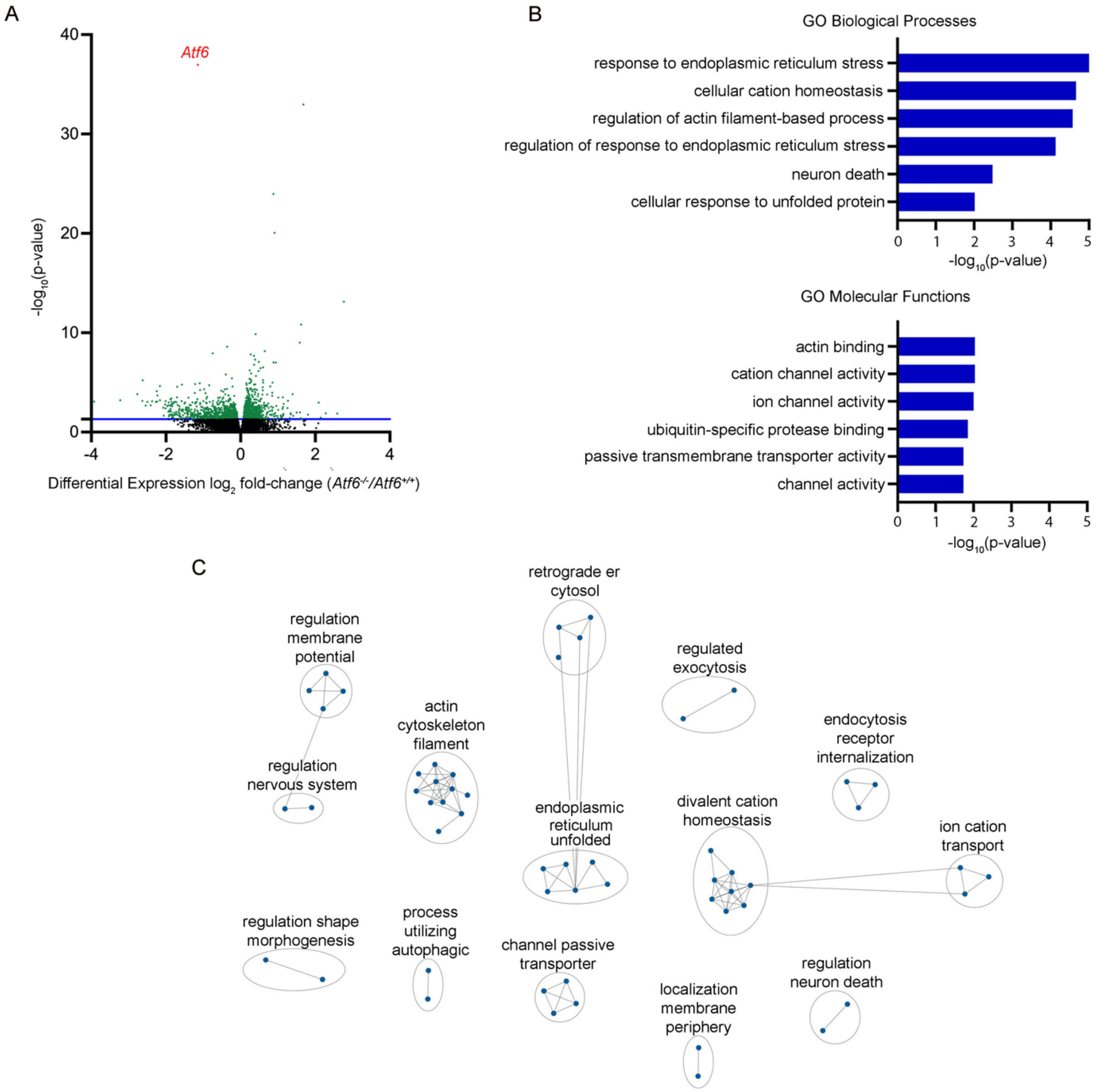

Figure 5. Gene expression in cochleae from 2-month-old *Atf6*$^{+/+}$ and *Atf6*$^{-/-}$ mice. (A) Volcano plot comparing transcript abundance between *Atf6*$^{+/+}$ and *Atf6*$^{-/-}$ cochleae. The number of DEGs is shown in green (n = 1,869), with the statistically significant cutoff ($p < 0.05$ and FC>0.05, above blue line). (B) Go analysis of 1869 DEGs via gProfiler reveals changes in ER stress, ion channel regulation, cell death, and actin filament organization. The y-axis shows -log10 p-value for the specified term. (C) Cytoscape network highlights key enriched themes in the *Atf6*$^{-/-}$ mice cochlea transcriptome. *Atf6* is indicated in red.

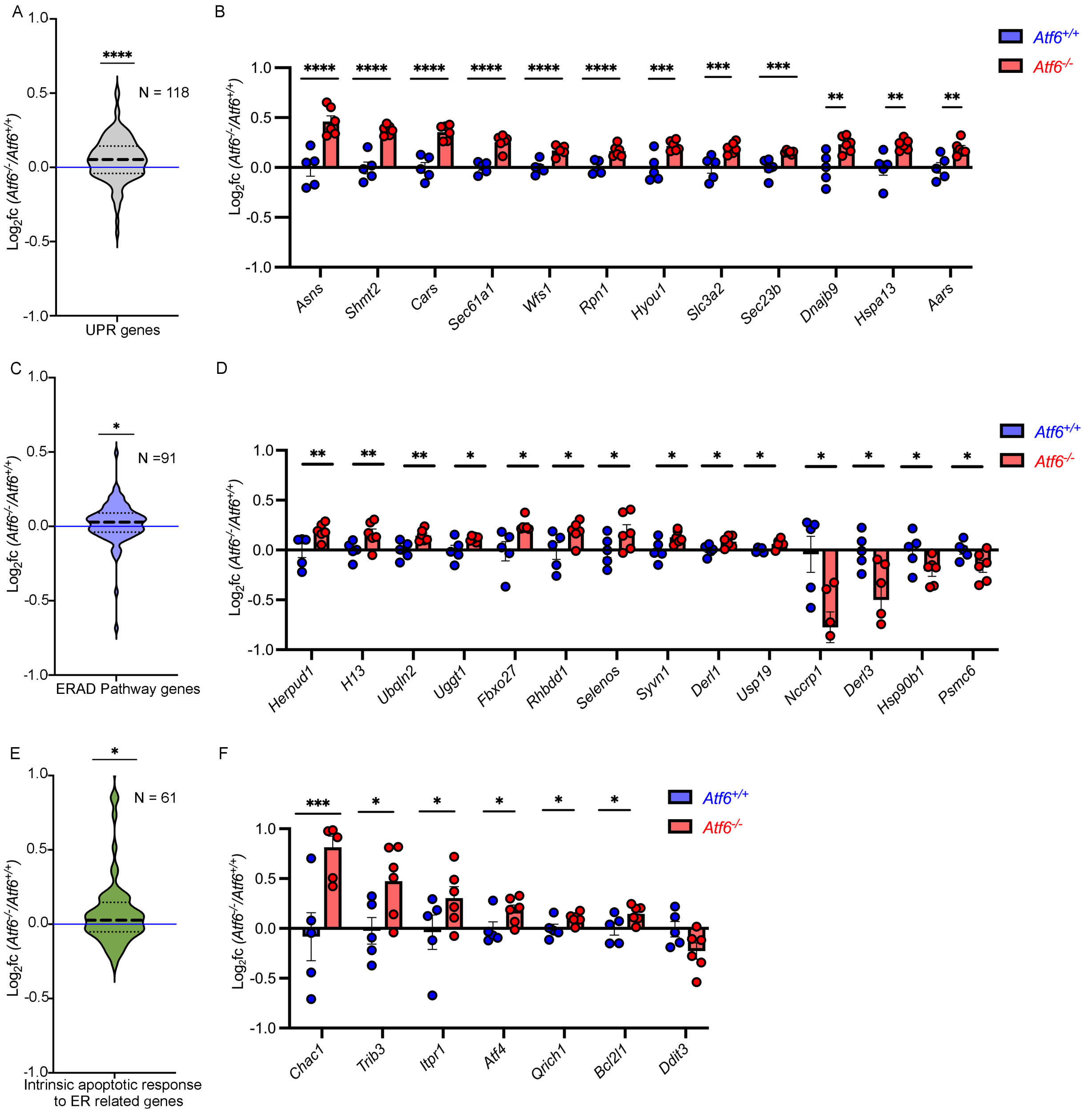

Figure 6. Up-regulation of ER stress genes in *Atf6*$^{-/-}$ cochlea. (A) Gray violin plot shows log2(fold changes) for 118 UPR-related genes in *Atf6*$^{-/-}$ vs. *Atf6*$^{+/+}$ cochlea (****p ≤ 0.0001, Wilcoxon Signed Rank Test; Supplemental Table 4). (B) Statistically significant UPR gene expression changes in *Atf6*$^{-/-}$ (red) vs. *Atf6*$^{+/+}$ (blue) cochleae, with error bars as mean ± SEM (**p ≤ 0.01, ***p ≤ 0.001, ****p ≤ 0.0001, DESeq2 analysis). (C) Blue violin plot shows log2(fold changes) for 91 ERAD genes (GO:0036503 “ERAD pathway”) in *Atf6*$^{-/-}$ cochlea (*p ≤ 0.05, Wilcoxon Signed

Rank Test; Supplemental Table 5). (D) Fourteen ERAD genes show statistically significant changes, with mean ± SEM (*p ≤ 0.05, **p ≤ 0.01, DESeq2, Supplemental Table 5). (E) Green violin plot shows log2(fold changes) of 61 intrinsic apoptotic genes (GO:0070059 “Intrinsic Apoptosis Response to ER stress”) in Atf6⁻/⁻ cochlea (*p ≤ 0.05, Wilcoxon Signed Rank Test; Supplemental Table 6). (F) Seven apoptotic genes show statistically significant expression changes, mean ± SEM (*p ≤ 0.05, ***p ≤ 0.001, DESeq2 analysis, Supplemental Table 6). Dashed lines in violin plots represent median and quartiles; the blue horizontal line shows log2fold = 0 (no change).

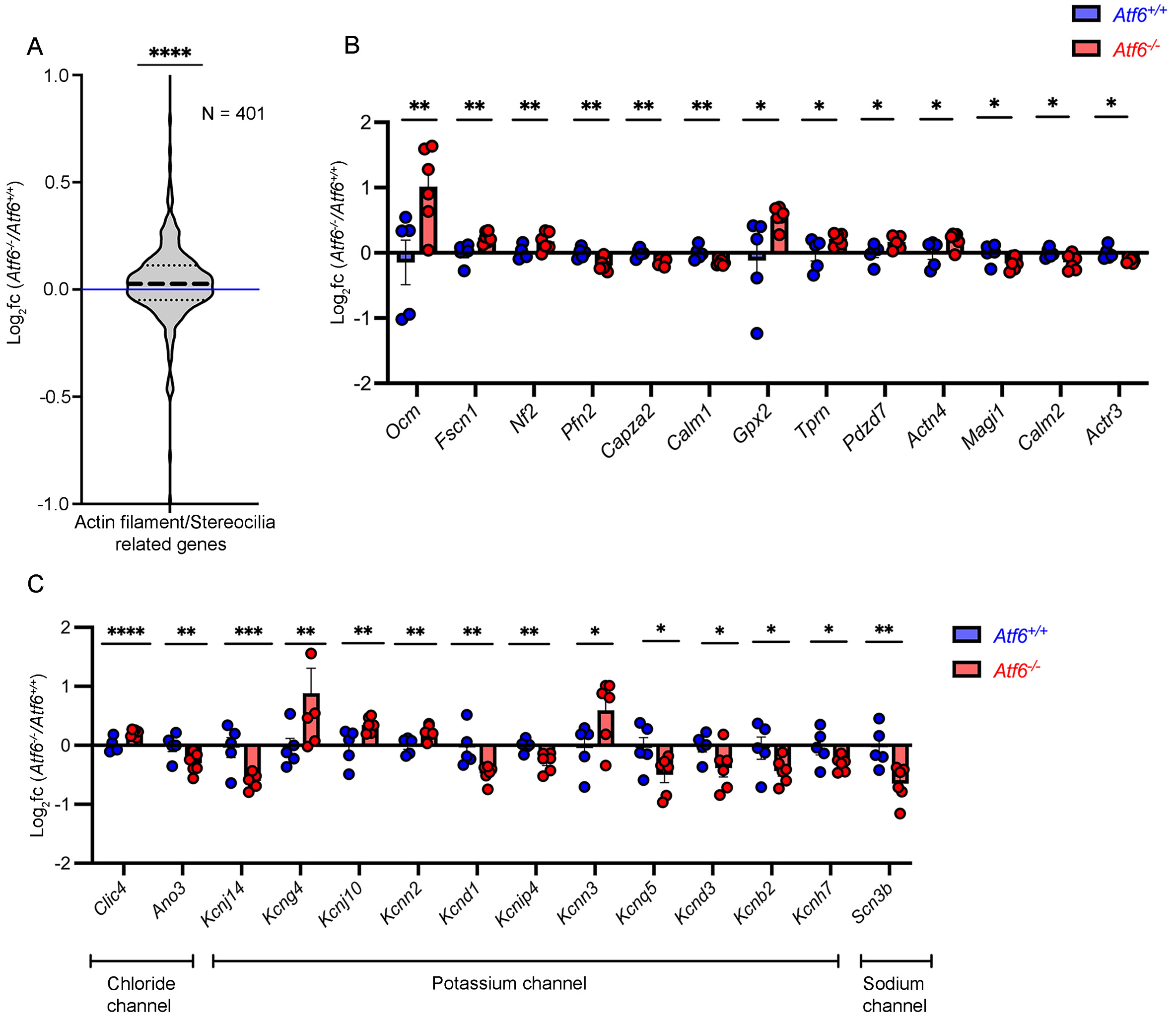

Figure 7. Dysregulated actin filament/stereocilia and channel-related gene expression in *Atf6*$^{-/-}$ cochlea. (A) Violin plots (gray) show log2(fold changes) in 401 actin filament/stereocilia-related genes in *Atf6*$^{-/-}$ vs. *Atf6*$^{+/+}$ cochlea transcriptomes (****$p \leq 0.0001$, Two-tailed Wilcoxon Signed Rank Test, Supplemental Table 8). Thick dashed line indicates median; thin dashed lines show quartiles, and the blue line shows no fold change. (B) Thirteen stereocilia genes show statistically significant changes between *Atf6*$^{-/-}$ (red) and *Atf6*$^{+/+}$ (blue), with error bars showing mean ± SEM (*$p \leq 0.05$, **$p \leq 0.01$, DESeq2 analysis, Supplemental Table 8). (C) Statistically significant changes in gene expression for chloride, potassium, and sodium channels in *Atf6*$^{-/-}$ vs. *Atf6*$^{+/+}$ cochleae are shown, with individual cochleae represented as circles and error bars as mean ± SEM (*$p \leq 0.05$, **$p \leq 0.01$, ***$p \leq 0.001$, ****$p \leq 0.0001$, DESeq2 analysis, Supplemental Table 9).